# Elastic constants of silicon materials calculated as a function of temperature using a parametrization of the second-generation reactive empirical bond-order potential

J. David Schall, Guangtu Gao, and Judith A. Harrison*

*Department of Chemistry, United States Naval Academy, Annapolis, Maryland 21402, USA*

(Received 14 February 2007; revised manuscript received 24 September 2007; published 24 March 2008)

A parametrization for silicon is presented that is based on the second-generation reactive empirical bond-order (REBO) formalism [Brenner, Shenderova, Harrison, Stuart, Ni, and Sinnott J. Phys.: Condens. Matter **14**, 783 (2002)]. Because it shares the same analytic form as Brenner's second-generation REBO, this new potential is a step toward a single potential that can model many atom systems that contain C, Si, and H, where bond breaking and bond making are important. The widespread use of Brenner's REBO potential, its ability to model both zero-Kelvin elastic constants of diamond and the temperature dependence of the elastic constants, and the existence of parameters for many atom types were the motivating factors for obtaining this parametrization for Si. While Si-C-H classical bond-order potentials do exist, they are based on Brenner's original formalism. This new parametrization is validated by examining the structure and stability of a large number of crystalline silicon structures, by examining the relaxation energies of point defects, the energies of silicon surfaces, the effects of adatoms on surface energies, and the structures of both liquid silicon and amorphous silicon. Finally, the elastic constants of diamond-cubic and amorphous silicon between 0 and 1100 K are calculated with this new parametrization and compared to values calculated using a previously published potential.

DOI: 10.1103/PhysRevB.77.115209 PACS number(s): 61.43.Bn, 62.20.D−, 62.20.F−

## I. INTRODUCTION

Because silicon has such a great technological importance, there have been many attempts to construct empirical potential energy functions to model its behavior. These potentials include, but are not limited to, the Stillinger and Weber (SW) potential,[1] three versions of the Tersoff potential [*T*1,[2] *T*2,[3] and *T*3[4]], the modified embedded atom method (MEAM),[5,6] and several other potentials.[5,7–14] Several extensive comparisons of these empirical potentials for silicon have appeared in the literature. For instance, Cook and Clancy[15] examined the behavior of the crystalline and liquid phases of Si using the MEAM potential and the modified version of the *T*3 potential (mod-*T*3).[16] In another study, Balamane, Halicioglu, and Tiller[17] performed a detailed comparison of six Si potentials, including the most popular SW and Tersoff potentials. They concluded that each of these potentials has strengths and weaknesses and that none of them is totally transferable.

Several attempts have been made to develop more transferable potentials. The environment-dependent interatomic potential (EDIP) has been developed for Si[12]) and for C.[18] The parameters were determined by fitting to a relatively small *ab initio* database. To test the transferability of the EDIP, the properties of amorphous and liquid silicon phases were examined. Although the liquid produced from the potential had some unphysical features, the distribution of bond angles is closer to the experimentally determined distribution than the distributions obtained with other potentials. The EDIP also provides a better description of amorphous silicon than other empirical potentials and produces reasonable amorphous structures from melt. Unlike most empirical potentials for Si,[12,17,19] the EDIP potential accurately describes the three elastic constants for diamond-cubic silicon, along with the Cauchy discrepancy $(C_{12}-C_{44})$. To its detriment, however, the bond lengths for the many of the crystalline silicon structures are overestimated. Recently a bond-order potential (BOP) for Si, which is based on the tight-binding description of covalent bonding, was developed.[14] This potential also does a reasonable job reproducing elastic constants and the Cauchy pressure of diamond-cubic silicon. As is the case with the EDIP, parametrizations have also been published for Si-Si and C-C interactions within this formalism but not for C-H, Si-H, and C-Si interactions.[20–22]

The Tersoff empirical potential energy functions,[2–4,16] first developed in 1986, were constructed to guarantee that the universal relation between binding energy and bond length put forth by Abell[23] was obtained. The bond-order potentials of Tersoff have spawned a number of other empirical potentials. For example, Brenner developed a reactive empirical bond-order (REBO) expression that describes hydrocarbon molecules and solid-state carbon on equal terms.[24,25] The main difference between Brenner's hydrocarbon REBO and Tersoff's carbon potential is the way in which the bond order is handled for hydrocarbon molecules, the pair-attractive and -repulsive terms remain the same. The REBO potential has proven to be very popular and has spawned additional potential development. The form of this potential was adopted by Murty and Atwater[26] to model Si-H systems and was then extended independently by Beardmore and Smith[8] and Dyson and Smith[11] to include C-Si-H interactions. In addition, Sbraccia, Silvestrelli, and Ancilotto[13] have modified Dyson and Smith's C-Si-H potential to improve its properties. Parametrizations also exist for Si-F,[27] Si-Cl,[27] and C-Pt.[28] With the exceptions of the T3, EDIP,[12] and BOP[14] the performance of most empirical potential energy functions in reproducing the zero-Kelvin elastic properties of diamond-cubic silicon is marginal.[19,29]

Despite the popularity of the original REBO, Brenner, Shenderova, Harrison, Stuart, Ni, and Sinnott[30] reported sev-

eral basic limitations of this potential. With these limitations in mind, they developed the second-generation REBO.[30] Among the many changes in the second version of potential, the form of the angular function was changed to provide a better fit to the elastic constants of diamond and graphite. The second-generation formalism also provides a significantly better description of bond energies, bond lengths, force constants, interstitial defect energies, and surface energies for diamond than its predecessor. In addition to being able to model the zero-Kelvin elastic constants of diamond, the second-generation REBO potential also predicts the correct qualitative trends in elastic constants, bulk modulus, and Cauchy pressure of diamond as a function of temperature.[31,32] In contrast, the original hydrocarbon REBO is unable to reproduce the correct qualitative trends in these properties as a function of temperature. Other potentials that share the same C-C functional form and parameters as the original REBO, such as the extended Brenner (XB) potential of Dyson and Smith[11] and the modified-extended Brenner (mXB) potential of Sbraccia, Silvestrelli, and Ancilotto,[13] are also unable to reproduce the correct qualitative trends in elastic constants of diamond with temperature.

Several types of covalent atoms have been parametrized within the second-generation REBO formalism. These include the C-H interactions derived by Brenner and coworkers,[30] and the C-O-H interactions derived by Sinnott and co-workers.[33] The second-generation REBO has been used extensively to model carbon nanotubes,[34–36] polycrystalline diamond structures,[37–39] and the tribology of amorphous carbon surfaces.[40,41] Given the types of covalent interactions that have already been parametrized, the ability to reproduce the zero-Kelvin elastic constants and the correct quantitative dependence of elastic constants on temperature, along with the widespread use of the Brenner potential, a parametrization for silicon (2B-Si) within the second-generation REBO formalism has been developed. The parametrization was generated using a fairly large database of experimental data and *ab initio* calculations consisting of bond lengths, energies, and elastic constants. The resulting parametrization provides a good description of bond lengths, energies, and bulk moduli for a wide range of crystal structures including those not used in the parameter fitting process. It accurately reproduces the energies and geometries of point defects in the bulk and in ideal and relaxed (100) $(1\times1)$ and $(2\times1)$ surfaces. It is also able to reproduce the energies of the ideal and relaxed (111) $(1\times1)$ surfaces. The 2B-Si parametrization is able to produce amorphous silicon structures that are in good agreement with experimentally determined properties and those from *ab initio* MD studies. In addition, it gives reasonable values for bulk modulus, the elastic constants, and the correct sign for the Cauchy discrepancy at zero-Kelvin and as a function of temperature. In this work, the results of extensive calculations on diamond-cubic silicon using the mXB potential also reported. These calculations confirm that the Si-Si portion of the mXB potential is unable to model the temperature dependence of the elastic properties of diamond-cubic silicon. This new parametrization for Si increases the number of atom pairs that have been parametrized for the second-generation REBO formalism. Ultimately, this should make it possible to use the second-generation REBO potential for large-scale simulations of a broad range of covalent materials.

This work is organized in the following way. The functional form of the second-generation REBO potential and the details of the parametrization of the attractive, repulsive, and the bond-order terms are presented first. The structures, bulk properties, interstitial defect energies, and surface energies of a large number of crystalline silicon structures have been calculated using this new parametrization and are presented next. In an effort to test the transferability of the potential, data for solid structures not included in the fitting database are also calculated. For comparison, these calculations also were conducted using the mXB potential. Data for EDIP and BOP potentials, when available, are provided for comparison. (Because extensive comparisons of other Si empirical potentials have appeared in the literature previously,[7,15,29,42,43] they are not included here.) Experiments show that amorphous silicon is composed of a random tetrahedral network of atoms. The ability of an empirical potential to reproduce the structure of amorphous silicon from quenching liquid silicon is an important test of any potential energy function. With that in mind, the structure of amorphous silicon obtained with the 2B-Si potential is compared with the experimentally determined structure. For completeness, the structural properties of liquid silicon are also calculated. For comparison, amorphous and liquid silicon structures were also generated using the mXB potential and the results of these calculations are presented. Finally, the new parametrization (2B-Si) for silicon is used to calculate the elastic moduli for diamond-cubic and amorphous silicon as a function of temperature and the results are compared to those obtained using mXB potential.

## II. METHOD

### A. Second-generation REBO potential

For an analytic potential energy function to be effective it must be flexible, accurate, transferable, and be computationally efficient. To date, analytic potentials with the highest degree of transferability are those that are based on sound quantum-mechanical bonding principles.[44] It can be shown that the bond-order potentials are based on the second-moment approximation.[44,45] The moments theorem states that the $n$th moment of the local density of states on an atom $i$ is determined by the sum of all paths between $n$ neighboring atoms that start and end at atom $i$. A good estimate of the bond energy can be obtained by knowing only the second moment, which is related to the energy beginning on atom $i$ and summing over the nearest neighbors.[45,46] Thus, the local electronic bond energy for each atom from molecular orbitals is proportional to the square root of the number of neighbors. Finnis and Sinclair[46] used this approximation to derive an expression for the energy of a solid in terms of pair-additive interactions between atoms. Their expression can be rearranged into an expression that is similar to the bond-order potentials.[44,45] Thus, the bond-order expressions of the "so-called" bond-order potentials capture the essence of quantum-mechanical bonding. It should also be noted that it is possible to derive other analytic forms based on higher

moments. For example, Pettifor and co-workers have developed a BOP that contains terms for $\sigma$ and $\pi$ bonding from the tight-binding model using the moments theorem.[20–22,47] Gillespie, Zhou, Murdick, Wadley, Drautz, and Pettifor recently developed parameters for Si-Si interactions within the BOP formalism.[14]

The total potential energy within the second-generation REBO formalism[30,44] is given by

$$E_b = \sum_i \sum_{j>i} [V^R(r_{ij}) - B_{ij} V^A(r_{ij})], \tag{1}$$

where $V^R$ and $V^A$ are pairwise repulsive and attractive contributions, respectively. The bond-order term $B_{ij}$ is a many-body term, which is related to the local environment of atoms $i$ and $j$. The pair potentials have the form

$$V^R(r) = f^c(r)(1 + Q/r)Ae^{-\alpha r}, \tag{2}$$

and

$$V^A(r) = f^c(r) \sum_{n=1,3} B_n e^{-\beta_n r} \tag{3}$$

for the repulsive and attractive pair terms, respectively, where $A$, $Q$, $\alpha$, $B_n$, and $\beta_n$ are fitting parameters. The screened Coulomb function used for the repulsive-pair interaction approaches infinity as interatomic distances approach zero. The attractive term has sufficient flexibility to simultaneously fit the bond energy and force constants. The function $f^c(r_{ij})$ is a continuous piecewise cutoff function that depends on the distance $r_{ij}$ between atoms $i$ and $j$ and is given by

$$f^c(r_{ij}) = \left\{ \begin{array}{ll} 1 & \text{for } (0, r_{\min}) \\ \frac{1}{2}\left[1 + \cos\left(\pi \frac{r - r_{\min}}{r_{\max} - r_{\min}}\right)\right] & \text{for } (r_{\min}, r_{\max}) \\ 0 & \text{for } (r_{\max}, \infty) \end{array} \right\}. \tag{4}$$

The bond-order $B_{ij}$ term is significantly different from both the Tersoff and the first-generation Brenner potential. Separate terms are included that depend on local coordination and bond angles, radical character and conjugation, and dihedral angle for carbon-carbon (C-C) double bonds. The bond-order term for the interaction between atoms $i$ and $j$ is given by

$$B_{ij} = \frac{b_{ij}^{\sigma-\pi} + b_{ji}^{\sigma-\pi}}{2} + (\Pi_{ij}^{RC} + b_{ij}^{DH}), \tag{5}$$

where $b_{ij}$, $\Pi_{ij}^{RC}$, and $b_{ij}^{DH}$ are the contributions to the bond-order arising from covalent bonding, conjugation, and dihedral torsions, respectively. The covalent-bond contribution is given as

$$b_{ij}^{\sigma-\pi} = \left[1 + \sum_{k\neq i,j} G_i(\cos(\theta_{jik}))e^{\lambda jik} + \text{corrections}\right]^{-1/2}. \tag{6}$$

The function $G(\cos(\theta))$ is approximated by fifth-order spline, which depends on the bond angle $\theta_{jik}$ between atoms $j$, $i$, and $k$, where atom $i$ is at the vertex of the angle. Following the procedure outlined by Brenner and co-workers, λ and the correction term are taken to be zero for silicon systems.[30]

### B. Fitting the Si-Si pair potential

The procedure outlined by Brenner and co-workers[30] was used to obtain parameters for the Si-Si pair potentials and angular terms. The pair terms [Eqs. (2) and (3)] contain nine parameters, $A$, $Q$, $\alpha$, $B_1$, $B_2$, $B_3$, $\beta_1$, $\beta_2$, and $\beta_3$. These values were optimized via least-squares minimization of an equation with the general form

$$Z = \sum_{n=1}^{M} |E(r_n) - E^\circ(r_n)|^2 + \sum_{n=1}^{M} |F(r_n) - F^\circ(r_n)|^2 + \sum_{n=1}^{M} |K(r_n) - K^\circ(r_n)|^2, \tag{7}$$

where $Z$ is the function to be minimized, $E$, $F$, and $K$ are the bond energy, force, and stretching force constant determined using Eq. (1), and its first and second derivatives, respectively, $M$ is the number of sets of data available in the fitting database, $r$ is the equilibrium bond length of structure $n$, and the symbol ° denotes the corresponding value for structure $n$ given from a fitting database. A simulated annealing algorithm implemented via the software package MATHEMATICA[48] was used to optimize the parameters. The database used for fitting these parameters and the values of the bond order consists of equilibrium distances, atomization energies, and stretching force constants for various silicon structures. Values for the properties in the database used for the fitting were determined the following way: Minimum-energy distances were taken from the literature and are tabulated in Table I. The force constants were either taken from the literature or calculated using the Badger-rule expression,

$$K = a(r_e - b)^{-3}, \tag{8}$$

where $K$ is the force constant, $r_e$ is the minimum-energy bond distance, and $a$ and $b$ are adjustable parameters. These two parameters were determined through least-squares fitting of minimum-energy distances and either force constant, bulk modulus, or vibrational frequency data found in the literature. Existing bond-additive values for determining molecular heats of formation of silanes generally include zero-point energies. For a classical potential, a new set of values, without zero-point energies, must be determined. To derive these, the heats of formation and zero-point energies for the molecules $Si_2H_6$, $Si_2H_4$, $Si_2H_2$, and $SiH_4$ were used to determine the molecular atomization energies. Assuming a constant value for the silicon-hydrogen bond, these atomization energies provide a complete set of data from which the bond-additive energies for the molecular silicon-silicon bonds can be derived.

To reduce the number of variables needed to fit both pair terms, initial guesses, which correspond to the C-C values from the second-generation REBO potential, were used for $A$, $Q$, and $\alpha$. Values for $B_1$, $B_2$, $B_3$, $\beta_1$, $\beta_2$, and $\beta_3$ were determined by a least-squares minimization of Eq. (1) and its first derivative using the equilibrium bond distance and energy from a Si-Si single bond. The equilibrium bond distance and energy of a Si-Si single bond were taken to be equal to the equilibrium bond length and bond energy of diamond-cubic silicon. The bond orders for first five structures in

TABLE I. Data used in the fitting scheme.

| Species | ΔH (eV)[a] | Zero-point energy (eV)[a] | Atomization energy (eV) | Si-Si bond energy (eV) | Si-Si bond distance (Å) | Si-Si force constant (Dyn/cm) |
|---|---|---|---|---|---|---|
| Diamond Cubic | | | 4.630[b] | 2.315 | 2.351[b] | 161241.3[e] |
| Hexagonal planar | | | 4.022[b] | 2.681 | 2.3[b] | 180642.1[f] |
| Simple cubic (SC) | | | 4.292[b] | 1.431 | 2.515[b] | 114515.4[e] |
| Body-centered cubic (BCC) | | | 4.191[b] | 1.048 | 2.635[b] | 95834.4[e] |
| Face-centered cubic (FCC) | | | 4.146[b] | 0.691 | 2.8[b] | 80232.4[e] |
| $SiH_4$ | 0.36 | 0.83 | 13.345[c] | | | |
| $Si_2H_2$ | 4.81 | 0.38 | 12.847[c] | 8.650 | 1.941[a] | 580460[g] |
| $Si_2H_4$ | 2.91 | 0.83 | 16.278[c] | 3.874 | 2.17[a] | 270446[h] |
| $Si_2H_6$ | 0.96 | 1.30 | 20.621[c] | 2.015 | 2.4[a] | 142697[i] |
| Si-H bond | 3.86 | 0.12 | 3.062[c] | 3.101 | | |
| Si-Si dimer | | | 1.565[c] | 3.130[d] | 2.24[d] | 222321.2[i] |

[a]From Ref. 49.
[b]From Refs. 50–52.
[c]Calculated assuming $\Delta H_{silicon}$=4.66 eV, $\Delta H_{hydrogen}$=2.26 eV. (Ref. 49).
[d]From Ref. 26.
[e]Calculated using bulk modulus values given in Ref. 53.
[f]Calculated using bulk modulus values given in Ref. 52.
[g]Calculated from the Si-Si stretch wave number given in Ref. 54.
[h]Estimated using Eq. (8) ($a$=288691 Å$^3$ dyn/cm, $b$=1.148 Å).
[i]Calculated from the Si-Si stretch wave number given in Ref. 26.

Table I were determined by setting the derivative of Eq. (1) equal to zero and solving for $B_{ij}$. For the remaining solid Si structures, bond energies and force constants were calculated at each structure's minimum-energy bond length using Eq. (1) or its second derivative, respectively. Two least-squares sums, one for the energies and another for the force constants were generated using the values in Table I. This sum was minimized by adjusting the three remaining parameters: $A$, $Q$, and $\alpha$. The values of $A$, $Q$, and $\alpha$ obtained from the minimization replaced the initial guesses and the entire process was repeated until a global minimum of the least-squares sum in Eq. (7) was reached. The final parameter values obtained through this procedure are shown in Table II. The cutoff parameters $r_{min}$ and $r_{max}$ were taken to be the same as those given by Sbraccia, Silvestrelli, and Ancilotto for the mXB potential.[13]

The repulsive and attractive pair terms calculated using the Si-Si parameters determined above are shown Fig. 1(a) as a function of interatomic distance. The total pair terms corresponding to the diamond-cubic, simple-cubic, and face-centered-cubic Si-Si bonds are shown in Fig. 1(b). The differences in these curves arise from the different bond-order terms for each solid silicon structure.

TABLE II. Parameters for the Si-Si pair terms in Eqs. (2) and (3).

| | | |
|---|---|---|
| $B_1$=92.74551 eV | $\beta_1$=1.72687 Å$^{-1}$ | $Q$=15.6614 Å |
| $B_2$=255.329 eV | $\beta_2$=1.64617 Å$^{-1}$ | $A$=90.1964 eV |
| $B_3$=−3.4026 eV | $\beta_3$=132.454 Å$^{-1}$ | $\alpha$=2.13083 Å$^{-1}$ |
| $r_{min}$=2.500 Å | $r_{max}$=3.050 Å | |

Using the Si-Si pair parameters and the pair potentials, the bond energy and force constants as a function of equilibrium bond distance were calculated (Fig. 2). For comparison, the bond energy and force constants calculated using the mXB potential are also shown in Fig. 2. The fitting data from Table I are indicated by the diamonds in each plot. It is clear from examination of Fig. 2 that the Si-Si parametrization presented here accurately describes bond energies, distances, and force constants. In contrast, the first-generation REBO potential is unable to describe these properties simultaneously. This deficiency is most notable at short bond lengths. It appears that the mXB potential attempts to strike some compromise between accurate bond energies and force constants.

### C. Fitting the bond order and $G(\cos(\theta))$

For the potential energy function to be able to model chemical reactions, where bond angles can change, an analytic form for the bond-order term must be available. This analytic form is obtained from fitting the discrete values of

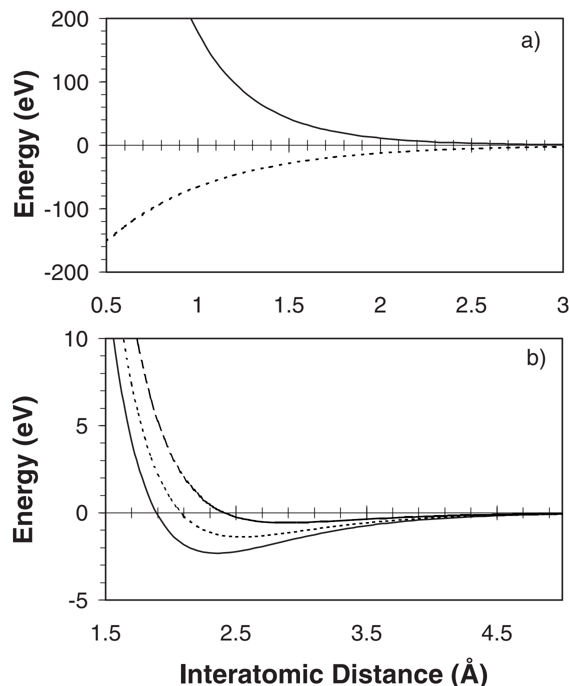


FIG. 1. (a) Pair-attractive (negative-dashed) and pair-repulsive (positive-solid) curves for the silicon parametrization of the second-generation REBO potential. (b) The total pair potential for a single Si-Si bond for the diamond-cubic (solid line), simple-cubic (short-dashed line), and face-centered-cubic (long-dashed line) phases of silicon. Potential truncation due to the cutoff function $f^c$ is not shown.

the bond-order to quintic-spline functions. In the case of Si, the $\pi$-bonding and dihedral terms in the empirical bond-order function [$\Pi^{RC}$ and $b^{DH}$ in Eq. (5)] are assumed to be zero. This is the approach used by many empirical Si potentials[29] and it is a reasonable assumption because Si typically forms single bonds. Thus, only the first term in Eq. (5) remains. In both the first- and second-generation REBO formalisms, this term is given by

$$b_{ij}^{\sigma-\pi} = \left[ 1 + \sum_{k \neq i,j} f_{ik}^{c}(r_{ik}) G_i(\cos(\theta_{jik})) e^{\lambda jik} \right]^{-1/2}, \qquad (9)$$

where $i$, $j$, and $k$ still refer to the atom identity and the function $f^c(r)$ ensures that the bond order only includes nearest-neighbor interactions.

The contribution that each neighbor makes to the empirical bond order is modulated by the $G(\cos(\theta))$ function according to the cosine of the angle of the bonds between atoms $i$ and $k$ and atoms $i$ and $j$. The procedure for determining the analytic form for the $G(\cos(\theta))$ function is described below. Because the diamond-cubic and hexagonal planar lattices contain only one angle each, 109.47° and 120°, respectively, Eq. (9) and the discrete values for the bond-order parameter can be used to yield the value of $G(\cos(\theta))$ at each angle. The values of $G(\cos(\theta))$ at 0° and 180° were estimated. The SC lattice contains both 180° and 90° angles; therefore, the $G(\cos(\theta))$ value at 90° was determined using the discrete bond order determined for SC lattice and the estimated $G(\cos(\theta))$ for 180°. For similar reasons, the value for $G(\cos(\theta))$ at 70.53° was determined using the discrete bond order for BCC solid silcon and the values of $G(\cos(\theta))$ at 109.47° and 180°. Finally, the value of $G(\cos(\theta))$ at 60° was determined using the discrete bond order for the FCC lattice and the $G(\cos(\theta))$ values at 90°, 120°, and 180°. Adjustments to the initial guesses of $G(\cos(\theta))$ at 0° and 180° were made and the process was repeated until the points comprising the discrete values of $G(\cos(\theta))$ fit a smooth function, which decreases as the bond angle increases.

Different quintic-polynomial splines in $\cos(\theta)$ were used in three regions of the bond angle $\theta$, $0° < \theta < 109.47°$, $109.47° < \theta < 120°$, and $120° < \theta < 180°$ to complete the $G(\cos(\theta))$ function. Because there are six spline coefficients, two values of the function and its first and second derivatives are needed in each region of the spline. The value of the second derivative of $G(\cos(\theta))$ at 109.47° was fit to the elastic constant $C_{11}$ for diamond-cubic silicon. The remaining first and second derivatives were chosen to suppress spurious oscillations in the splines and to fit the discrete values of $G(\cos(\theta))$ at bond angles in-between the spline nodes. The complete set of splines that compose the $G(\cos(\theta))$ function are shown in Fig. 3 and the coefficients of these splines are given in Table III.

## III. RESULTS AND DISCUSSION

### A. Crystalline silicon structures

The equilibrium lattice parameters, cohesive energies, and bulk moduli calculated using the new second-generation REBO parametrization (2B-Si) for Si are shown in Table IV. Values from the first-principles calculations or from experiment, values calculated using the mXB potential, and available data obtained using both the EDIP and the BOP are also included for comparison. The values obtained with the EDIP and the BOP are included here because both potentials do a reasonable job reproducing the zero-Kelvin elastic constants for diamond-cubic silicon. In addition, the EDIP produces an amorphous structure from the melt that is similar to the structure obtained from *ab initio* MD simulations. Because detailed comparisons of many other empirical Si potentials, e.g., SW, T2, and T3,[7,15,29] have appeared previously in the literature, comparisons to those potentials are not included in Table IV.

Both the new 2B-Si parametrization and the mXB potential do an excellent job reproducing cohesive energies and lattice constants. With the exceptions of the diamond-cubic, SC, and the $\beta$-Sn structures, the EDIP produces bond lengths that are slightly longer than the experimental values. The 2B-Si and the mXB potentials also do a reasonable job reproducing bulk moduli of the structures that were used in the parametrization, i.e., diamond, hexagonal planar, SC, BCC, and FCC. The elastic constants of the diamond-cubic structure were used in the fitting of the EDIP. Because the bulk modulus and two elastic constants are related via the relation $B = \frac{1}{3}(C_{11} + 2C_{12})$, the EDIP also reproduces the bulk modulus of this structure. Bulk moduli calculated with the EDIP are not available for the other crystalline silicon structures. The bulk modulus obtained using the BOP is also reasonably

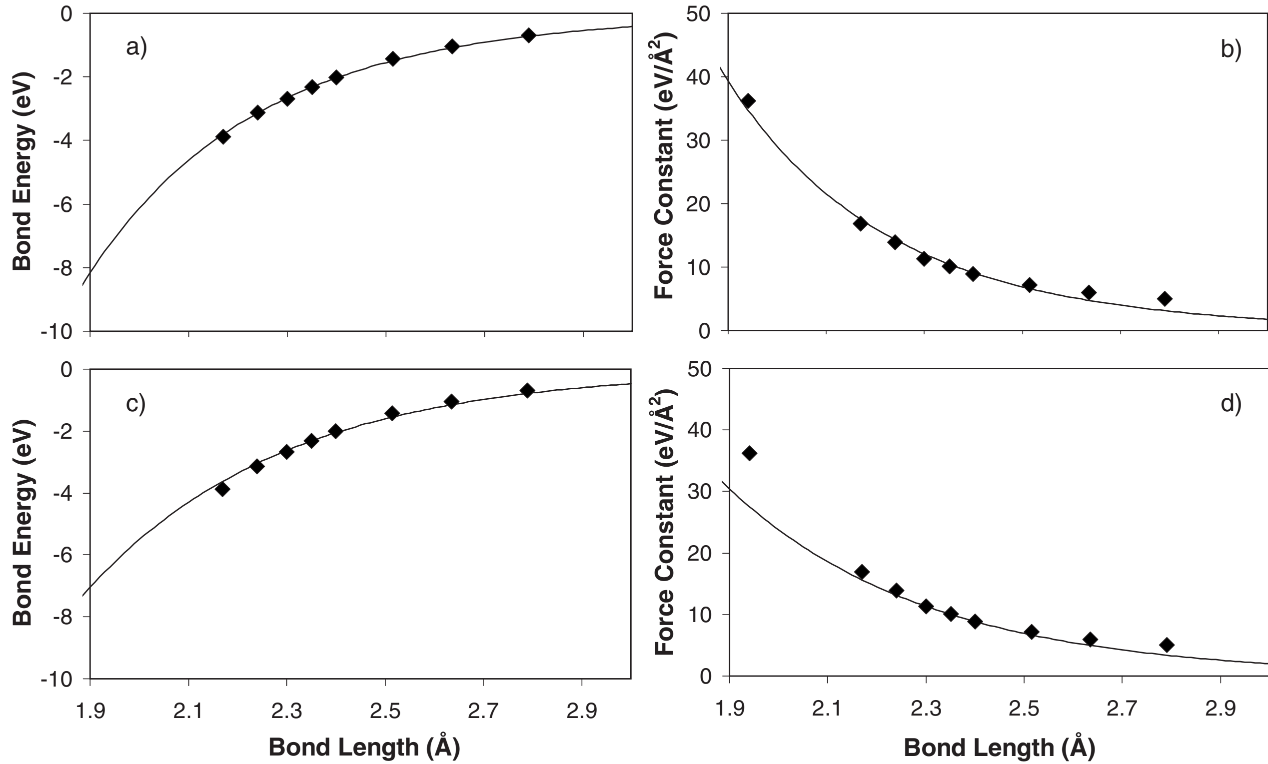


FIG. 2. Plots of bond energy and force constant as a function of bond length for the Si-Si pair terms for the 2B-Si [(a) and (b)] and mXB [(c) and (d)] potentials.

close to the experimental value despite underestimating $C_{11}$ by 21%. The 2B-Si potential, the EDIP, and the BOP are able to reproduce the zero-Kelvin elastic constants for the diamond-cubic structure. The mXB potential is able to reproduce the bulk modulus for the diamond structure because it reproduces the force constant of the Si-Si bond. However, it fails to accurately predict the zero-Kelvin elastic constants for the diamond-cubic structure which are more closely linked to the angular dependence of the potential.

Silicon has a negative Cauchy discrepancy ($C_{12}-C_{44}$).[55] The values of $C_{12}-C_{44}$ are −14 GPa from experiment, −41 GPa from the 2B-Si potential, and +55 GPa for the mXB potential, respectively. The 2B-Si potential, the EDIP, and the BOP are among the few empirical silicon potentials that produce a negative Cauchy discrepancy. (For an explanation of how the Cauchy discrepancy can be fit within the BOP formalism see Ref. 56.) Because most empirical potentials underestimate $C_{44}$, these potentials are also unable to reproduce the negative Cauchy discrepancy. While the Cauchy discrepancy does not have any physical implications for crystal stability, the values of the individual elastic constants are important for crystal stability. In the case of zero applied stress, there are three elastic stability criteria: $C_{11}+2C_{12}>0$, $C_{44}>0$, and $C_{11}-C_{12}>0$.[57] The first is related to the bulk modulus, the second to the shear modulus, and the third is related to the modulus against tetragonal shear. While all of the common empirical potentials for silicon meet these criteria, most of these potentials significantly underestimate the value of $C_{44}$.[19,29] Because the 2B-Si was fit to $C_{11}$ and the bulk modulus of diamond-cubic silicon, it also accurately reproduces $C_{12}$. The value of $C_{44}$ was not used in the fitting

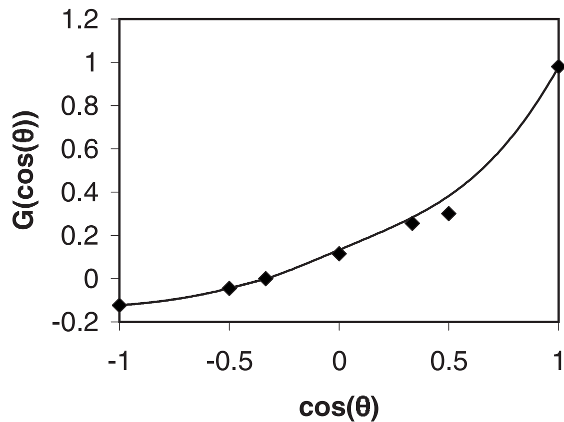


FIG. 3. The angular contribution to the bond-order expression. Diamonds are the fitting data derived from the discrete bond-order values and the solid line is the quintic-spline function with nodes at $\theta=180°$, 120°, 109°, and 0° [$\cos(\theta)=-1$, $-1/2$, $-1/3$, and 1].

TABLE III. Parameters for the angular contribution to the silicon bond order.

| $\cos(\theta)$ | $G(\cos(\theta))$ | $dG/d(\cos(\theta))$ | $d^2G/d(\cos(\theta))^2$ |
|---|---|---|---|
| −1 | −0.122736935 | 0.065720000 | 0.320763152 |
| −1/2 | −0.044734259 | 0.249121746 | 0.380715536 |
| −1/3 | −0.000223579 | 0.308832492 | 1.125000000 |
| 1 | 0.980000000 | 1.800000000 | 2.610000000 |

TABLE IV. Equilibrium lattice parameters ($a_0$ and $c_0$) in Å, cohesive energy relative to diamond-cubic silicon ($\Delta E$) in eV, and bulk modulus ($B$) in GPa from experiment and *ab initio* calculations (Exp/*ab*), the second-generation REBO parametrization (2B-Si) and the modified-extended Brenner (mXB) potential. Available data for the environment-dependent interatomic potential (EDIP) and Gillespie's bond-order potential (BOP) are also shown for comparison. The zero-Kelvin elastic constants for silicon in the diamond structure (in GPa) and Si-Si dimer bond length, bond energy, and force constant $K$ (in dyn/cm) are also given.

| Lattice | | Exp/*ab*[a] | 2B-Si[b] | mXB[b] | EDIP[c] | BOP[d] |
|---|---|---|---|---|---|---|
| Diamond cubic | $a_0$ | 5.429 | 5.429 | 5.429 | 5.43 | 5.43 |
| | $E$ | −4.63 | −4.63 | −4.63 | −4.65 | −4.63 |
| | $B$ | 101.9 | 102.9 | 98.2 | 99 | 92.29 |
| | $C_{11}$ | 171.5 | 176.0 | 109.2 | 175 | 134.89 |
| | $C_{12}$ | 67.1 | 66.3 | 93.0 | 62 | 70.98 |
| | $C_{44}$ | 81.1 | 108.0 | 38.0 | 71 | 84.03 |
| | $C_{44}^0$ | 111[e] | 138.5 | 28.5 | 112 | |
| | $C_{11}$-$C_{12}$ | 104.4 | 109 | 16.2 | 113 | 63.91 |
| | $C_{12}$-$C_{44}$ | −14 | −41.7 | 55.0 | −9 | −13.05 |
| Si dimer | $r_0$ | 2.24[f] | 2.24 | 2.24 | | |
| | $E$ | −3.13[f] | −3.10 | −3.05 | | |
| | $K$ | 222321[f] | 227204 | 210636 | | |
| Hexagonal planar | $a_0$ | 3.984 | 3.984 | 3.995 | 4.018 | |
| | $\Delta E$ | 0.61 | 0.64 | 0.76 | 0.640 | |
| | $B$ | 50[g] | 58.3 | 56.0 | | |
| SC | $a_0$ | 2.515 | 2.545 | 2.510 | 2.503 | |
| | $\Delta E$ | 0.34 | 0.50 | 0.36 | 0.532 | 0.20 |
| | $B$ | 105.6[h] | 86.9 | 86.3 | | 126.43 |
| BCC | $a_0$ | 3.042 | 3.076 | 2.947 | 3.243 | |
| | $\Delta E$ | 0.44 | 0.61 | 0.76 | 1.594 | 0.60 |
| | $B$ | 111.3[h] | 84.2 | 74.2 | | 74.09 |
| FCC | $a_0$ | 3.960 | 3.944 | 3.761 | 4.081 | |
| | $\Delta E$ | 0.48 | 1.26 | 2.62 | 1.840 | 0.55 |
| | $B$ | 93.54[h] | 46.3 | 40.7 | | 80.95 |
| $\beta$-Sn[i,j] | $a_0/c_0$ | 4.828/2.634 | 4.819/2.629 | 4.698/2.563 | 4.76/− | |
| | $\Delta E$ | 0.21 | 0.42 | 0.39 | 0.67 | |
| | $B$ | 129.1[h] | 145.5 | 105.4 | | ∼90[l] |
| BC8[i,j] | $a_0$ | 6.640 | 6.657 | 6.621 | | |
| | $\Delta E$ | 0.11 | 0.32 | 0.15 | | |
| | $B$ | 96.4[h] | 97.3 | 365.7 | | ∼102[l] |
| BCT5[i,j] | $a_0/c_0$ | 5.959/3.312 | 6.072/3.375 | 6.066/3.372 | −/3.36 | |
| | $\Delta E$ | 0.23 | 0.26 | 0.14 | 0.26 | |
| | $B$ | 111.4[k] | 121.4 | 119.7 | | |

[a]Values for diamond-cubic silicon are from experiment. Energies and lattice constants are from the DFT/LDA calculations of Yin and Cohen[51,52], unless otherwise noted.
[b]Calculated in this work.
[c]From Ref. 12.
[d]From Ref. 14.
[e]The DFT/LDA calculation for $C_{44}^0$ is from Ref. 61.
[f]For the Si dimer from Ref. 26.
[g]From Ref. 52.
[h]From Refs. 53 and 62.
[i]These structures were not included in the database used to fit the potential.
[j]DFT/LDA from Refs. 61 and 63.
[k]DFT/LDA from Ref. 62.
[l]Estimated from Fig. 3 of Ref.14.

procedure and the potential overestimates this value. The BOP accurately reproduces $C_{12}$ and $C_{44}$ but underestimates $C_{11}$. In contrast, the EDIP potential uses all three of the elastic constants in the fitting procedure and reproduces these values well.[12] In the case of finite strain, the elastic stability criteria take slightly different forms depending upon the type of applied stress.[58] For example, under hydrostatic pressure ($P$) the stability criteria are given by $(C_{11}+2C_{12})/3-P/3 > 0$ (spinodal criterion), $C_{44}-P>0$ (shear criterion), and $(C_{11}-C_{12})/2-P>0$ (Born criterion). Therefore, empirical potentials that significantly underestimate $C_{44}$, as most existing potentials do, may not be stable under large hydrostatic pressures.

To test the transferability of the 2B-Si potential, equilibrium lattice parameters, cohesive energies, and bulk moduli were calculated for several metastable structures of silicon ($\beta$-Sn, BC8, and BCT5), which were not included in the fitting database (Table IV). The $\beta$-Sn structure is a body-centered tetragonal unit cell with a two-atom basis. The angles between the four-nearest neighbors are 149° and 94°. The BC8 structure is a BCC lattice with an eight-atom basis with two bond angles of 117.9° and 99.2°.[59] The theoretical BCT5 structure is a body-centered tetragonal lattice with fivefold coordination.[60] Cartesian coordinates for each unit cell can be obtained from http://cst-www.nrl.navy.mil/lattice/. Of the three potentials where data are available (2B-Si, mXB, and EDIP), the 2B-Si potential performs slightly better when predicting the equilibrium lattice parameters of all three structures. The $\beta$-Sn is somewhat problematic for both the mXB potential and the EDIP with both potentials predicting lattice constants that are short compared to the DFT value. None of the three potentials is able to accurately predict the cohesive energy of the $\beta$-Sn structure. Both the 2B-Si and the mXB potentials predict a change in energy ($\Delta E$) that is approximately two times larger than the experimentally determined value while the EDIP value is about three times larger. The cohesive energies for the BCT5 and the BC8 structures are mixed. The predictions for the cohesive energy of the BCT5 structure obtained with the 2B-Si potential and the EDIP are equal and very close to the DFT value. In contrast, the cohesive energy obtained with the mXB potential is not large enough. In the case of the BC8 structure, the mXB potential does the best job reproducing the cohesive energy while the value obtained with 2B-Si potential is too large. The values obtained for the bulk moduli of these three structures using mXB and the 2B-Si potentials differ markedly. While the 2B-Si potential does a reasonable job predicting the bulk moduli of these structures, the mXB potential does not. In fact, the value of the bulk modulus for the BC8 structure predicted with mXB is about 3.5 times too large.

To be useful, a potential energy function must predict the most stable thermodynamic structure. For solid silicon, the diamond-cubic structure is the lowest energy structure. Examination of the data in Table IV for the 2B-Si potential reveals that the diamond-cubic structure has the lowest cohesive energy of the ordered structures listed. To insure that there are no disordered Si structures with a lower energy than the diamond-cubic structure, the energies of disordered structures must be examined. Following the general method outlined by Brenner,[30] a system consisting of 1000 Si atoms was melted at 3500 K and then slowly cooled to 10 K over a period of 10 ns in a constant pressure ensemble. Once cooled to 10 K, the potential energy was minimized using a steepest descent algorithm.[64] The average cohesive energy of the system was found to be −4.400 eV/atom or 0.23 eV higher than diamond-cubic silicon and the density was 2.29 g/cm$^3$, 2.1% lower than the diamond-cubic structure. Examination of many amorphous structures generated with the 2B-Si, using by various procedures, strongly suggests that diamond-cubic silicon is indeed the most stable form of solid silicon.

TABLE V. Relaxed energies (eV) of point defects in diamond-cubic silicon. *Ab initio* (DFT/LDA) data are given as a range of reported values for the formation energy of the ideal structure and relaxation energy $\Delta E^{\mathrm{relax}}$ of the relaxed structure (in parentheses).

| | 2B-Si | mXB | EDIP[a] | BOP[b] | DFT/LDA[c] |
|---|---|---|---|---|---|
| $V$ | 3.98 | 4.03 | 3.22 | 2.759 | 3.3–4.3 (0.4–0.6) |
| $I_T$ | 4.55 | 3.24 | 4.05 | 2.846 | 3.7–4.8 (0.1–0.2) |
| $I_H$ | 4.00 | 2.45 | 4.16 | 2.636 | 4.3–5.0 (0.6–1.1) |

[a]From Ref. 19.
[b]From Ref. 14.
[c]From Ref. 53.

The formation energy of point defects governs their concentration. Because point defects are more mobile than perfectly bonded atoms, diffusion in silicon is dominated by point defects.[53] Therefore, the formation energy is an important property. Calculated values of the relaxation energies of two interstitial defects in diamond-cubic silicon, the tetrahedral ($I_T$) and the hexagonal ($I_H$), and the vacancy are shown in Table V. (Available data obtained with the EDIP and the BOP are also shown for comparison.) The point-defect energies were calculated at zero pressure by iteratively relaxing the atomic coordinates via a steepest descent algorithm and adjusting the cubic periodic box dimensions via a golden section search routine until the change in total energy between iterations reached a tolerance level of $\Delta E=1\times 10^{-8}$ eV.[64] A small cell containing $64\pm 1$ atoms with cubic periodic boundaries was used to simulate a bulk environment. The reference is a perfect diamond-cubic Si lattice. The formation energy $E_f$ is given by[29]

$$E_f = E - (N \pm 1)E_c,$$

where $E$ is the total simulation energy of $N\pm 1$ atoms, +1 for an interstitial and −1 for a vacancy, and $E_c$ is the bulk cohesive energy of diamond-cubic silicon.

It is clear from examination of Table V that the relaxation energies calculated with the 2B-Si potential and the EDIP are very close to the range of values reported from DFT calculations. In contrast, two of the energies obtained with the mXB potential and all three of the values obtained with the BOP fall outside the DFT ranges.

### B. Free surfaces

Due to their importance to the microelectronics industry, the (100) and (111) surfaces of Si have been studied exten-

TABLE VI. Selected properties of Si(100) surfaces. $\gamma$ is the surface energy, $\Delta\gamma$ is the relative energy with respect to the ideal $(1\times1)$ surface, $\Delta$ is the first interlayer contraction (in %), $r_d$ and $r_{bb}$ are the bond lengths (in Å) of the dimer and the back bond between surface and second-layer atoms, and $\theta_1, \theta_2, \theta_3$ are the bond angles as indicated in Fig. 4. Energies are in units of eV/$(1\times1)$ cell. Unless otherwise noted, DFT results are from Refs. 29 and 53 and references therein. (Data have not been published for the EDIP or BOP.)

| | 2B-Si | mXB | DFT |
|---|---|---|---|
| | Ideal $(1\times1)$ | | |
| $\gamma$ | 2.31 | 2.28 | 2.50 |
| | Relaxed $(1\times1)$ | | |
| $\Delta\gamma$ | −0.04 | −0.02 | −0.03 |
| $\Delta$ | −6.62 | −5.15 | −5.10 |
| | $(2\times1)$ | | |
| $\Delta\gamma$ | −0.76 | −0.85 | −0.93 |
| $\Delta$ | −6.41 | −4.57 | −24.40 |
| $r_d$ | 2.35 | 2.30 | 2.23 |
| $r_{bb}$ | 2.33 | 2.35 | 2.29 |
| $\theta_1$ | 108.6° | 108.3° | 107.8° |
| $\theta_2$ | 91.6° | 92.6° | 92.9° |
| $\theta_3$ | 106.1° | 104.9° | 100.8° |

sively. (For a review of these surfaces, see Ref. 65.) The properties of free surfaces are important for surface growth and etching. Because these surfaces exhibit a large number of reconstructions and the geometry of the surface atoms differs from the bulk, they provide another interesting test for the transferability of any empirical potential. The surface energies of the ideal and relaxed (100) $(1\times1)$ surface calculated with the 2B-Si and the mXB potentials are shown in Table VI. For comparison, available DFT data are also shown. Both potentials produce surface energies that are within 9% of the DFT value with the 2B-Si value being a bit closer to the DFT value. The reduction in surface energy and the surface contraction for the relaxed structure is also predicted by both potentials. It should also be noted, however, that the percentage contraction obtained using the mXB potential is closer to the DFT value.

A number of models have been proposed to explain the experimentally determined surface patterns on the (100) surface. Images obtained using scanning tunneling microscopy

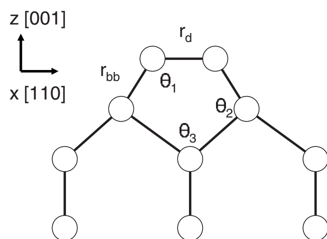


FIG. 4. Side view of the Si(100) $(2\times1)$ surface showing the symmetric dimer configuration. Indicated on the figure are bond lengths and angles given in Table VI.

TABLE VII. Selected properties of Si(111) surfaces. $\gamma$ is the surface energy, $\Delta\gamma$ is the relative energy with respect to the ideal $(1\times1)$ surface, $\Delta$ is the first interlayer contraction (in %) and $r_{a2}$ is the distance between adatoms and the second layer (in Å). Energies are in units of eV/$(1\times1)$ cell. DFT/LDA results are from Refs. 2, 29, 62, 68, and 73.

| | 2B-Si | mXB | DFT/LDA |
|---|---|---|---|
| | Ideal $(1\times1)$ | | |
| $\gamma$ | 1.16 | 1.49 | 1.56 |
| | Relaxed $(1\times1)$ | | |
| $\Delta\gamma$ | −0.11 | −0.12 | −0.17 |
| $\Delta$ | −24.0 | −16.5 | −27.0 |
| | $(\sqrt{3}\times\sqrt{3})H_3$ | | |
| $\Delta\gamma$ | 0.30 | −0.52 | −0.07 |
| $r_{a2}$ | 1.91 | 2.31 | 2.12 |
| | $(\sqrt{3}\times\sqrt{3})T_4$ | | |
| $\Delta\gamma$ | 0.69 | −0.37 | −0.28 |
| $r_{a2}$ | 2.58 | 2.48 | 2.49 |
| | $(2\times2)$ $H_3$ hexagonal | | |
| $\Delta\gamma$ | 0.21 | −0.46 | −0.24 |
| $r_{a2}$ | 1.99 | 2.05 | |
| | $(2\times2)$ $T_4$ hexagonal | | |
| $\Delta\gamma$ | 0.48 | −0.39 | −0.24 |
| $r_{a2}$ | 2.58 | 2.48 | |
| | $(2\times2)$ $H_3$ rectangular | | |
| $\Delta\gamma$ | 0.20 | −0.48 | −0.17 |
| $r_{a2}$ | 1.96 | 2.01 | |
| | $(2\times2)$ $T_4$ rectangular | | |
| $\Delta\gamma$ | 0.48 | −0.39 | −0.28 |
| $r_{a2}$ | 2.58 | 2.48 | |

have confirmed that the dimer model is correct.[66,67] Dimerization occurs when two surface atoms, initially in their ideal (100) positions, move toward each other along the [110] direction (Fig. 4). The surface dangling bonds then form a bond. This structure is known as the $(2\times1)$ reconstruction. Figure 4 shows the symmetric dimer structure which appears in defect-free surfaces.[66,67] However, when defects are present, the dimer is buckled and asymmetric and causes subsurface atomic displacements that extend four layers into the bulk. Both the mXB and the 2B-Si potential predict that the $(2\times1)$ reconstructed surface is lower in energy than the ideal or relaxed structures in agreement with the DFT calculations. In fact, most empirical potentials, except for the T2 potential, predict a change in surface energy for this reconstruction that is in agreement with the DFT value.[29] The change in surface energy predicted from the mXB potential is closer to the value predicted by DFT calculations while the first-layer contraction predicted by the 2B-Si potential is closer to the DFT value.

With the exception of the $\theta_3$ (Fig. 4), the remaining distances and bond angles are reproduced reasonably well by both potentials. It should be noted that values for the angle $\theta_3$ obtained with most other empirical potentials more closely match the DFT value. Because the buckling of the dimer is a

quantum-mechanical phenomenon, all of the previously published empirical potentials produce a symmetric dimer structure.[29]

The predicted surface energies for the ideal Si(111) $(1\times1)$ surface using the mXB and the 2B-Si potentials, as well as the DFT values, are shown in Table VII. Balamane, Halicioglu, and Tiller showed that all six of the empirical potentials they examined underestimated the surface energy of the ideal Si(111) $(1\times1)$ surface.[29] This is also the case with the mXB and the 2B-Si potentials. The energy produced using the mXB potential yields the closest value to the DFT value followed by the 2B-Si, which gives a similar energy as the SW potential. When the surface is relaxed, both empirical potentials examined here yield a lower energy and the value is in reasonable agreement with the DFT value. This is not the case for all empirical potentials. The energy decrease predicted by the $T2$ and $T3$ potentials is not nearly large enough, while the SW potential predicts no decrease at all.[29] The 2B-Si potential does a better job reproducing the surface contraction of the relaxed surface than the mXB potential.

On the $(1\times1)$ surface, adatoms can be placed in a tetrahedral site directly over a second-layer atom $(T_4)$ or in a tetrahedral site directly over a hollow $(H_3)$.[68] Both $(2\times2)$ (hexagonal and rectangular) and $(\sqrt{3}\times\sqrt{3})$ surface reconstructions are possible. The surface energies of all the possible adatom structures calculated using DFT and the local density approximation (LDA) are lower than the ideal $(1\times1)$ surface energy. Meade and Vanderbilt have assigned this energy difference to different electronic structures of the surfaces.[69] Recent DFT calculations that utilize the Perdew-Burke-Ernzerhof generalized gradient approximation and Gaussian basis functions obtain the same trend in surface energies as obtained with LDA/DFT calculations; however, the $(2\times2)$ $H_3$ and $(\sqrt{3}\times\sqrt{3})$ $H_3$ structures were less stable than the ideal $(111)(1\times1)$ surface.[70] Recent nonorthogonal tight binding (TB) calculations obtain values for the surface energies of the $(2\times2)$ $H_3$ and the $(2\times2)$ $T_4$ structures in good agreement with the early DFT/LDA values.[53]

The surface energies obtained with the mXB and the 2B-Si potentials for the adatom surface reconstructions discussed above are shown in Table VII. Only the mXB potential correctly predicts that all the adatom structures are more stable than the ideal $(1\times1)$ surface. The only other empirical potential to predict the correct sign of the surface energies relative to the ideal $(1\times1)$ surface is the $T2$ potential.[29,71] However, the relative ordering of the adatom structures predicted by both the $T2$ and the mXB potentials is different from the DFT/LDA results. The 2B-Si potential, like the majority of empirical Si potentials, is unable to predict the lowering of the surface energy in the presence of adatoms on the $(1\times1)$ surface. Despite this, it correctly predicts the first-interlayer contraction.

Balamane, Halicioglu, and Tiller suggest that the competition between the energy gain associated with a reduction in the number of dangling bonds and the strain caused by the very small bond angles present in these adatom structures will dictate the stability of the adatom structures.[29] They conclude that because the bond-bending forces in the $T2$ potential are small, it provides a better description of surface energies in these systems than potentials with larger bond-bending forces, such as the $T3$ potential. In the same way, the bond-bending forces in the mXB potential are weaker than the 2B-Si potential; thus, it provides a better description of the surface energies of adatom structures. It should be noted that these structures can be accurately modeled. For example, Khor and Das Sarma[72] modified the angular portion of their earlier potential so that adatom energies could be accurately modeled. However, the Khor and Das Sarma potential does not allow the character of the bonds to change as the atoms move in a simulation.

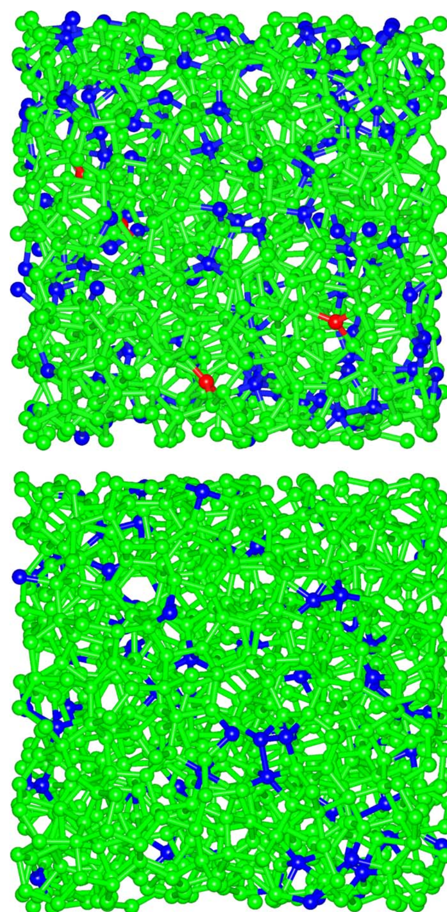

FIG. 5. (Color online) Ball and stick representation of $a$-Si generated using the mXB (lower panel) potentials and the 2B-Si (upper panel) potentials. The atoms have been colored by their coordination number. Red, green, and blue spheres indicate threefold, fourfold, and fivefold coordination, respectively.

### C. Amorphous silicon

A particularly stringent test of the transferability of the potential is how well it can reproduce properties of amorphous silicon ($a$-Si) because no information about $a$-Si was included in the fitting procedure used here. Several amorphous structures were generated by melt and quench techniques. Two structures (Fig. 5) were generated from the melt using a method similar to that described by Tersoff.[4] A system of 1000 Si atoms was equilibrated at 3500 K using a constant-pressure ensemble. Over a period of 125 ps, the

TABLE VIII. Density ($\rho$), first- ($R_1$) and second-neighbor ($R_2$) peak distance from the radial distribution, average coordination number ($C_1$) and average bond angle ($\theta$), FWHM values for the bond angle distribution, and zero-Kelvin elastic constants in GPa for crystalline Si (*c*-Si) from experiment and *a*-Si from experiment and simulation using the 2B-Si, mXB, and EDIP potentials. FWHM is the full width at half maximum.

| | Experiment *c*-Si | Experiment *a*-Si | 2B-Si *a*-Si | mXB *a*-Si | EDIP[e] |
|---|---|---|---|---|---|
| $\rho$ (g cm$^{-3}$) | 2.34 | 2.11–2.29[b] | 2.29 | 2.29 | 2.255 |
| $R_1$ (Å) | 2.356[a] | 2.352[c] | 2.356 | 2.356 | 2.369 |
| $R_2$ (Å) | 3.841[a] | 3.81[c] | 3.819 | 3.873 | 3.809 |
| $C_1$ (atoms) | 4.021[a] | 3.881[c] | 4.11 | 4.07 | 4.05 |
| $\theta$ (FWHM) | 109.5° [a] | 108.6° (11°) | 108.5° (26°) | 108.5° (38°) | 108° (18°) |
| $C_{11}$ | 171.5 | 156[d] | 138.8 | 113.6 | |
| $C_{12}$ | 67.1 | 58.4[d] | 71.1 | 76.3 | |
| $C_{44}$ | 81.1 | 48.8[d] | 33.7 | 18.6 | |

[a]Determined from radial distribution function generated from powder diffraction experiment.[83,84]
[b]Range of values reported from various sources.[83–86]
[c]Determined from analysis of radial distribution function for annealed *a*-Si.[83,84]
[d]From Ref. 87.
[e]From Ref. 12.

system was cooled to 1000 K at constant pressure. Once the system reached equilibrium, it was cooled to 300 K and equilibrium established again. For comparison, a second system was generated using identical simulation conditions and the mXB potential (also shown in Fig. 5). No artificial methods, such as the bond-switching method,[74] were required to generate these amorphous structures. It should be noted that only a small number of empirical Si potentials, e.g., EDIP and now the 2B-Si, are able to produce a physically reasonable amorphous structure by quenching liquid Si.

The radial distribution function, density, average coordination number, and bond-angle distributions were calculated for both of the structures in Fig. 5 and the results are shown in Table VIII. The average coordination number ($C_1$) is given by

$$C_1 = \frac{1}{n}\sum_i \sum_{j\neq i} f_{ij}^c. \tag{10}$$

For comparison, available data for structures generated using the EDIP potential are also shown.[12] The density, first- and second-neighbor distances, and average bond angle for the *a*-Si structures generated with the 2B-Si potential, mXB potential, and the EDIP are all in excellent agreement with experimental data.

All three of the potentials predict an average coordination number that is slightly higher than the experiment. The 2B-Si and the mXB produce 13.5% and 6.7% fivefold coordinate defects (also referred to as *T*5 or floating-bond defects), respectively. The 2B-Si potential also predicts a small number of threefold coordinate defects (0.4%) (also referred to as *T*3 or dangling-bond defects). No *T*3 defects were present in *a*-Si created using the mXB potential. There are some experimental results and high level *ab initio* MD simulations that indicate both *T*3 and *T*5 defects may be present in *a*-Si.[75–80] To what degree *T*5 defects are present, and what role they play in *a*-Si properties, is still a subject of debate[71,79,81,82] and it is not possible to experimentally detect these defects.

It is also interesting to note that when the quench rate was reduced from ~300 K/ps to ~0.350 K/ps the percentage of *T*5 defects was reduced from 13.5% to 4.8% while the number of *T*3 defects was approximately constant when the 2B-Si potential was used. This same trend was apparent in structures produced from *ab initio* MD simulations.[80] This suggests that the high value of average coordination obtained in the MD simulations may be related to the limitations on quenching rate or annealing time.

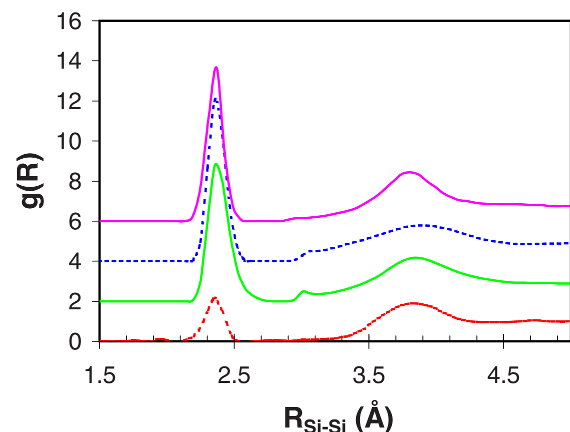


FIG. 6. (Color online) Radial distribution functions for *a*-Si at 300 K. In order from the top of the figure, distributions obtained using the EDIP[12] (pink solid), the mXB potential (blue dashed), the 2B-Si (green solid), and from experiment[83,84] (red dashed) are shown. These data are normalized so that $g(\infty)=1$ and the curves are offset from the experimental curve by 2, 4, and 6 units, respectively, on the $y$ axis for clarity.

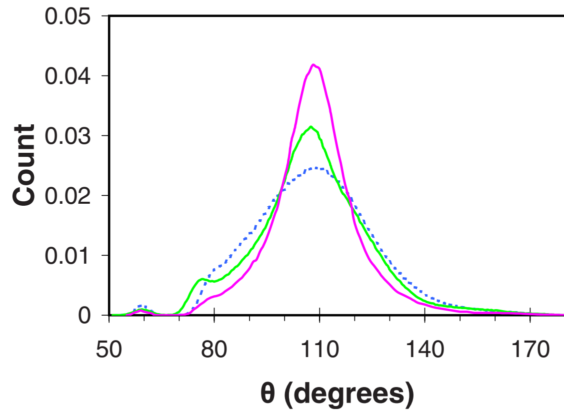


FIG. 7. (Color online) Bond-angle distributions of *a*-Si at 300 K. At the most probable angle, the topmost distribution was obtained using the EDIP (pink) followed by the 2B-Si (green) and the mXB potential (blue) distributions. The distributions have been normalized by the total number of counts.

The radial distribution functions for the *a*-Si structures generated using both potentials are shown in Fig. 6. For comparison, the experimentally determined radial distribution function for an ion-implanted, annealed *a*-Si[83,84] and the function generated using the EDIP[12] are also shown. It is clear from examination of this figure that all three potentials predict the correct placement of the first- and second-neighbor peaks relative to experiment. The intensities of the first-neighbor peaks generated with the three potentials are nearly equal and approximately twice as intense as the experimentally determined data. In contrast, both the EDIP and the 2B-Si potential accurately reproduce the intensity of the second-neighbor peak while the mXB potential does not.

The bond-angle distribution in experimentally produced annealed *a*-Si is determined to be 108.6° with a full width at half maximum (FWHM) of 11.0°,[78] which is near the ideal tetrahedral bond angle of 109.5°. The calculated bond-angle distributions for the *a*-Si structures generated using the 2B-Si and mXB potentials are shown in Fig. 7. The data for the EDIP are also shown for comparison.[12] Both the 2B-Si and the mXB distributions have maxima at a bond angle of 108.5°, while the distribution generated using the EDIP is centered about 108.0°.

The 2B-Si generated *a*-Si has a narrower angle distribution with a FWHM value of 26°, whereas the distribution generated using the mXB potential has a fairly broad peak with a FWHM value of 38°. This suggests that the 2B-Si potential generates *a*-Si with a higher level of tetrahedral ordering. The distributions generated with both potentials have small peaks at 60°. The distribution generated using 2B-Si potential also has a small shoulder at 78°. Both of these peaks are due to the presence of *T*5 defects. Further analysis of the bond angles indicates that the *T*3 defects found in the 2B-Si generated *a*-Si have an average bond angle of 119.5°, which indicates that their geometry is nearly planar. In contrast, the geometry predicted for *T*3 dangling-bond defects predicted by *ab initio* calculations is nearly tetrahedral.[88]

TABLE IX. Liquid Si: Density ($\rho$), first- ($R_1$) and second-neighbor ($R_2$) peak distance from the radial distribution, average coordination number ($C_1$), and average bond angle ($\theta$) for the bond-angle distribution for liquid silicon from experiment and simulation using the 2B-Si, mXB, and EDIP potentials.

| | Experiment | 2B-Si | mXB | EDIP[a,b] |
|---|---|---|---|---|
| $\rho$ (g cm$^{-3}$) | 2.533 | 2.17 | 2.29 | 2.255 |
| $R_1$ (Å) | 2.46 | 2.41 | 2.41 | 2.46 |
| $C_1$ (atoms) | $6.4 \pm 0.5$ | 3.89 | 4.33 | 4.5 |
| $\theta$ | | 105.5° | 99.0° | 100° |

[a]From Ref. 91.
[b]From Ref. 12.

### D. Liquid silicon

While the 2B-Si potential was not developed to model liquids, examining the performance of this potential for liquid Si provides another interesting test of its transferability. Most empirical Si potentials are unable to fully describe the liquid phase.[12,89] Two existing empirical potentials (SW and MFF[90]) that are able to describe the liquid phase of Si with varying levels of success were each fit to reproduce the melting point. The SW potential also reproduces the pair-correlation function of the liquid;[1,89] however, it does not reproduce the *ab initio* bond-angle distribution.[80,89]

Another potential that has had some success describing the liquid phase of Si is the *T*3 potential. The radial distribution function generated with the *T*3 potential is in general agreement with the experimentally determined function with the first peak appearing at 2.45 Å compared to the experimental value of 2.533 Å (Table IX). The density of the liquid increases by 4% upon melting; however, the melting point predicted by the *T*3 potential (~3000 K) is almost twice as

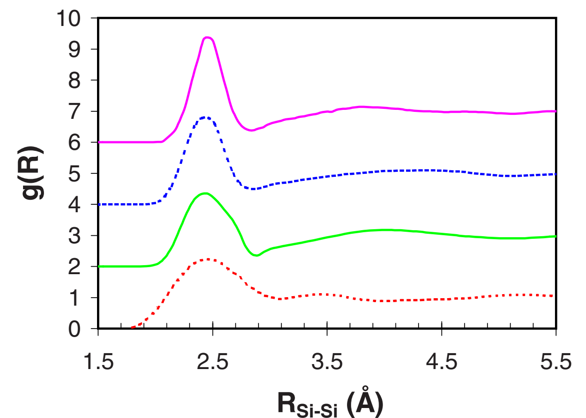


FIG. 8. (Color online) Radial distribution functions for liquid Si. In order from the top of the figure, distributions obtained at 1800 K using the EDIP[12] (pink solid), at 3500 K using the mXB potential (blue dashed), at 3500 K using the 2B-Si (green solid) potential, and from experiment[91] (red dashed) at 1829 K are shown. These data are normalized so that $g(\infty)=1$ and the curves are offset from the experimental curve by 2, 4, and 6 units, respectively, on the $y$ axis for clarity.

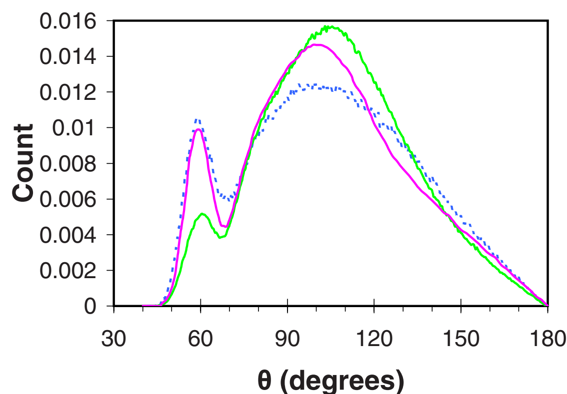


FIG. 9. (Color online) Bond-angle distributions for liquid Si. In order from the top of the figure for the peak near 109°, distributions obtained using the 2B-Si (green), the EDIP (pink), and the mXB potential (blue). The distributions have been normalized by the total number of "counts" and the temperatures are the same as in Fig. 8.

large as the experimentally determined value (1685 K). In addition, the number of neighbors found by integration of the radial distribution function up to the first peak is 4.5, while the experimentally determined number is 6.4.

The radial distribution functions for liquid silicon obtained using 2B-Si potential, the mXB potential, the EDIP,[12] and the experimentally determined function[91] are shown in Fig. 8 and other liquid data are summarized in Table IX. Note, these distributions were obtained at different temperatures). The level of agreement between these functions and the experimental data is surprising in view of the fact that none of these potentials were fit to liquid-phase properties. The width of the first peak generated with all the empirical potentials is too narrow. The peak in the function produced using the EDIP potential has the narrowest distribution. The EDIP potential is able to do a reasonable job modeling the melting temperature of silicon. It produces a value which is 20% lower than the experimental value while the other empirical potentials, e.g., 2B-Si (3140 K) and mXB (2190 K), predict melting temperatures which are too large. Finally, only the $T3$ potential correctly predicts the density of silicon will increase upon melting. The EDIP, 2B-Si, and mXB potentials all predict a slight decrease in the density upon melting (Table IX).

The distribution of bond angles within liquid silicon is another important quantity to examine (Fig. 9). The EDIP,[12] mXB, and the 2B-Si potentials all capture the bimodal shape of the bond-angle distribution present in the *ab initio* MD distribution.[80] However, the most probable peak produced by the three empirical potentials is shifted toward the tetrahedral angle while the most probable peak is closer to 90° in the *ab initio* MD distribution.

### E. Elastic properties as a function of temperature of *dc*-Si and *a*-Si

Elastic constants can be calculated from molecular dynamics simulations at finite temperature by the direct method, which involves calculating elastic constants from a stress-strain curve,[92] and fluctuation methods, which make use of ensemble averages of the fluctuations in either strain or stress.[32,93–99] For crystals with cubic symmetry, there are only three independent elastic constants, $C_{11}$, $C_{12}$, and $C_{44}$. For isotropic materials, such as the *a*-Si structures examined here, the number of independent elastic constants is reduced to two, $C_{11}$ and $C_{12}$, where $C_{44}=(C_{11}-C_{12})/2$.[100]

Recently, the direct, stress-fluctuation and strain-fluctuation methods were used to calculate the elastic constants of diamond as a function of temperature.[31] Each of these methods has advantages and disadvantages.[32] For example, using the strain-fluctuation method for the elasticity tensor requires the use of variable box-size MD simulations and the simulations can be slow to converge.[101,102] In contrast, the stress-fluctuation method for calculating the stress and elasticity tensors can be implemented in the constant-volume ensemble. A drawback of this method is that the second derivative with respect to strain of the interatomic potential must be evaluated which can be challenging for multibody potentials. In a recent work, the first and second derivatives of the second-generation REBO potential with respect to strain were derived and equations that can be used to obtain these derivatives for all angular-dependent potentials were presented.[32]

The direct method in a constant-strain ensemble was used to calculate elastic constants as a function of temperature reported herein. For the elastic moduli of diamond-cubic silicon, the simulation cell is constructed such that the edge vectors of the cell are parallel with an edge of the unit cell of the diamond lattice, with [100] along $x$, [010] along $y$, and [001] along $z$.[31] To determine the elastic constants $C_{11}$ and $C_{12}$, the simulation box is scaled along the $x$ direction by a factor of $1+e$, where $e$ is the compression ratio. For small values of e , the system is under a strain of

$$\varepsilon_{ij} = \begin{vmatrix} e & 0 & 0 \\ 0 & 0 & 0 \\ 0 & 0 & 0 \end{vmatrix} + \delta_{ij}, \tag{11}$$

where $\delta_{ij}$ is the $3\times 3$ identity matrix. This leads to the relationships for $\sigma_{xx}$ and $\sigma_{yy}+\sigma_{zz}$ given by Gao *et al.*,[31] which can be used to determine $C_{11}$ and $C_{12}$. In a constant-volume simulation, the corresponding stresses, $\sigma_{xx}$, $\sigma_{yy}$, and $\sigma_{zz}$ can be found from the ensemble averages of the internal stress tensor. We have recently shown that the internal stress tensor can be calculated for multibody potentials.[32]

To determine $C_{44}$ for cubic crystal structures, the crystal must be rotated such that one side of the periodic simulation cell corresponds to a [110] plane with two edges along ⟨110⟩ directions and the third orthogonal direction along a ⟨100⟩ direction. Thus, $x'$ is along [110], $y'$ is along [$\bar{1}$10], and $z'=z$ is along the [001] direction, where the primes denote the rotated reference frame. This is equivalent to a 45° rotation of the crystal about the $z$ axis. If a strain of $1+e$ is applied along the $x'$=[110] direction, then the pressure on the (110) plane $P_{110}$ can be calculated in a constant-volume simulation from $\sigma_{x'x'}$. The equation relating $P_{110}$ to the three elastic constants can then be used to obtain $C_{44}$.[31]

When there are only two independent elastic constants, as is the case with the amorphous or isotropic systems, $C_{44}$ can be calculated using $C_{11}$ and $C_{12}$. However, $C_{44}$ can also be obtained from the simulation and then used to determine the degree of anisotropy in a system, which gives a measure of the quality of amorphous structure. The anisotropy factor is defined as

$$A = 1 - \frac{C_{44}}{\frac{1}{2}(C_{11} - C_{12})}, \tag{12}$$

where $C_{11}$, $C_{12}$, and $C_{44}$ are all determined directly from simulation. When $A$ equals 0, the system will be isotropic. Unfortunately, the method described above for calculating $C_{44}$ fails for isotropic and amorphous systems because they do not have the convenient axes of symmetry required for rotations. In this case, an equivalent strain tensor and resolved stress must be found. In the reference frame of the rotated, (110)-oriented system, the strain tensor can be written in matrix form as

$$\varepsilon'_{ij} = \begin{vmatrix} e & 0 & 0 \\ 0 & 0 & 0 \\ 0 & 0 & 0 \end{vmatrix} + \delta_{ij}. \tag{13}$$

The strain tensor can be rotated back into the original (100)-oriented reference frame by rotating by −45° about the $z$ axis using Euler's rotation theorem.[103]

$$\varepsilon = \ell_z \varepsilon' \ell_z^T, \tag{14}$$

where

$$\ell_z = \begin{vmatrix} \cos(\gamma) & \sin(\gamma) & 0 \\ -\sin(\gamma) & \cos(\gamma) & 0 \\ 0 & 0 & 1 \end{vmatrix}, \tag{15}$$

and superscript $T$ is the matrix transpose. For a −45° rotation about the $z$ axis the equivalent strain in the original, unrotated reference frame is given by

$$\varepsilon_{ij} = \begin{vmatrix} e/2 & e/2 & 0 \\ e/2 & e/2 & 0 \\ 0 & 0 & 0 \end{vmatrix} + \delta_{ij}. \tag{16}$$

The stress on any plane in a body is given by $\mathbf{P}=\mathbf{n}\sigma$, and the stress normal to the plane is given as $\sigma_N=\mathbf{nP}$, where $\mathbf{n}$ is the unit vector of the plane defined by its crystallographic indices divided by the vector norm. For the (110) plane,

$$P_{110} = \sigma_N = \tfrac{1}{2}(\sigma_{11} + 2\sigma_{12} + \sigma_{22}). \tag{17}$$

Thus, the three elastic constants and the anisotropy factor can be calculated by applying the appropriate strain to the simulation box. First, $C_{11}$ and $C_{12}$ are determined. The resolved stress $P_{110}$ is found via Eq. (17) using the internal stress tensor and substituted into $P_{110}$ that relates the three elastic constants, which is then rearranged to solve for $C_{44}$. The nonorthogonal periodic boundary conditions which arise from the application of the strain in Eq. (16) are handled using the minimum image convention.[104]

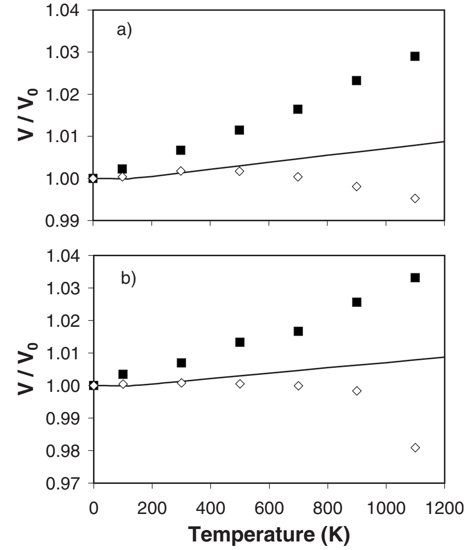


FIG. 10. Volume change as a function of temperature for diamond-cubic silicon (a) and $a$-Si (b) as calculated with the 2B-Si (squares) and mXB (open diamonds) potentials. In both plots, the solid line is the experimentally determined volume change for diamond-cubic silicon replotted from Ref. 109.

The direct method requires that the simulations be conducted in a canonical ($NVT$) ensemble. Because the system volume is a function of temperature, this dependence must be determined to ensure that all stresses calculated as a function of applied strain are relative to the zero-stress condition. For this reason, a series of MD simulations using the isothermal-isotension ensemble (TtN)[96] were conducted. During a simulation, the computational cell is allowed to change shape and size and the shape of the simulation cell is a dynamic variable.[105] The simulation cell is constructed from three time-dependent vectors **a**, **b**, and **c**. The matrix $h$ is formed from these three vectors such that $h=(\mathbf{a},\mathbf{b},\mathbf{c})$. A technique suggested by Nosé and Klein is applied to maintain the symmetry of the $h$ matrix, and thus prevents system rotations.[106] The simulations are performed with the thermodynamic tension and external hydrostatic pressure set to zero. In most of the simulations presented here, the simulation system contains 1000 silicon atoms. Dynamic equations are integrated using a fourth-order Gear predictor-corrector algorithm with a constant time step size of 0.25 fs.[107] Temperatures are controlled using Nosé's extended-system method.[108]

The systems are equilibrated for a minimum of 200 ps. The instantaneous values of the $h$ matrix are averaged over the course of the simulation to obtain an average box shape $h_0$. The $h_0$ matrix indicates that the diamond-cubic silicon structures generated with both the 2B-Si and the mXB potentials remain orthogonal and cubic after equilibration. A small amount of nonorthogonality is introduced into the $a$-Si samples after equilibration. The average volume, calculated by taking the determinant of the $h_0$ matrix is plotted as a function of temperature in Fig. 10. The volume has been normalized by each system's volume at zero Kelvin. The volume at zero Kelvin was determined by minimizing the

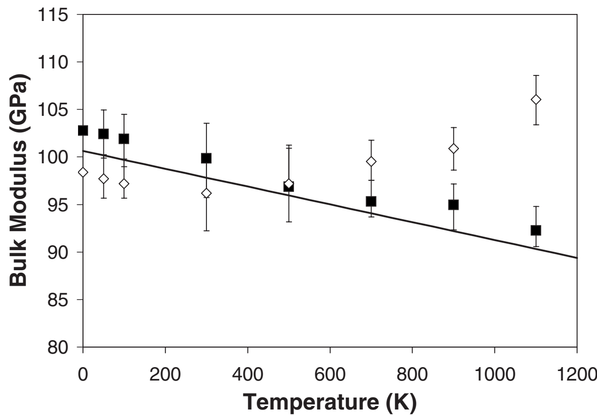


FIG. 11. Bulk modulus calculated for 2B-Si (squares) and mXB (open diamonds) diamond-cubic silicon. The error bars indicate high and low values. The solid line represents the experimental values.[111] For cubic systems the bulk modulus is given by $B=\frac{1}{3}(C_{11}+2C_{12})$.

potential energy by adjusting the simulation box size. The figure shows results for diamond-cubic silicon [Fig. 10(a)] and $a$-Si [Fig. 10(b)] calculated with both the 2B-Si and the mXB potentials. For comparison, experimental data for diamond-cubic silicon are also shown.[109] The 2B-Si potential predicts that volume expansion increases almost linearly with temperature for both diamond cubic and $a$-Si. This trend agrees qualitatively with the experimentally determined values. However, the experimentally determined values do not show as strong of a dependence on temperature.

An average volumetric thermal expansion coefficient was determined by taking the slope of the relative volume $(V/V_0)$ versus temperature over the temperature range of 50–1100 K. The experimentally determined value for diamond-cubic silicon is $8.2\times10^{-6}$ K$^{-1}$ compared to a value of $2.7\times10^{-5}$ K$^{-1}$ and $3.0\times10^{-5}$ K$^{-1}$ for the 2B-Si diamond cubic and $a$-Si, respectively. The volume calculated using the mXB potential at first appears to increase and then begins to contract unrealistically as temperature continues to increase and no attempt was made to approximate a thermal expansion coefficient.

The elastic constants of diamond-cubic silicon as a function of temperature calculated with the 2B-Si potential are shown in Figs. 11 and 12. For comparison, values calculated using the mXB potential and the experimental values are also shown. The bulk modulus calculated with the 2B-Si potential decreases with increasing temperature and is in qualitative and reasonable quantitative agreement with the experimental bulk modulus. The mXB potential is in good agreement at low temperatures (<300 K) but begins to increase in a nonphysical way above 300 K. Both $C_{11}$ and $C_{44}$ decrease slightly with increasing temperature and this trend is qualitatively reproduced by the 2B-Si potential. However, the calculated $C_{11}$ values decrease more markedly than the experimentally determined values with the difference between the two values becoming larger as the temperature is increased. The "fast softening" of the elastic constants $C_{11}$ and $C_{44}$ with temperature predicted by MD simulations has been previously observed for diamond[31] and is a direct consequence of the inability of classical MD simulations to accurately predict thermal expansion. These results are explained by Gruneisen's law, which states that the higher the thermal expansion coefficient, the faster the elastic softening.[110]

Because the value of $C_{44}$ calculated with the 2B-Si potential at 0 K is larger than the experimental value, the values of $C_{44}$ calculated with the 2B-Si potential approach the experimental values as the temperature is increased. In contrast, the mXB potential predicts that both $C_{11}$ and $C_{44}$ are fairly insensitive to temperature. In addition, the values of these elastic constants calculated with the 2B-Si potential are much closer to the experimentally determined values. The experimentally determined values of $C_{12}$ decrease slightly over the temperature range considered. The 2B-Si potential values show a slight increase at small temperatures and then are fairly insensitive to the changes in temperature. Coincidentally, with the 2B-Si potential, the fast softening of $C_{11}$ and the increase in $C_{12}$ combine to give the correct temperature response for the bulk modulus shown in Fig. 11. The $C_{12}$ values calculated using the mXB potential show an initial decrease with increasing temperature and then begin to rise

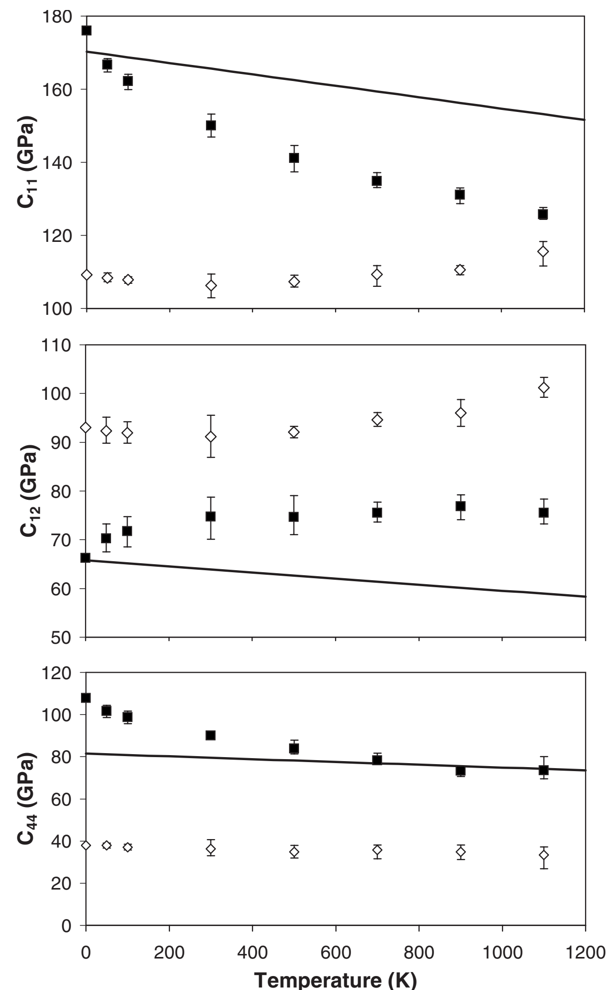


FIG. 12. Elastic constants calculated for 2B-Si (squares) and mXB (open diamonds) diamond-cubic silicon. The error bars indicate high and low values. The solid line represents the experimental values.[111]

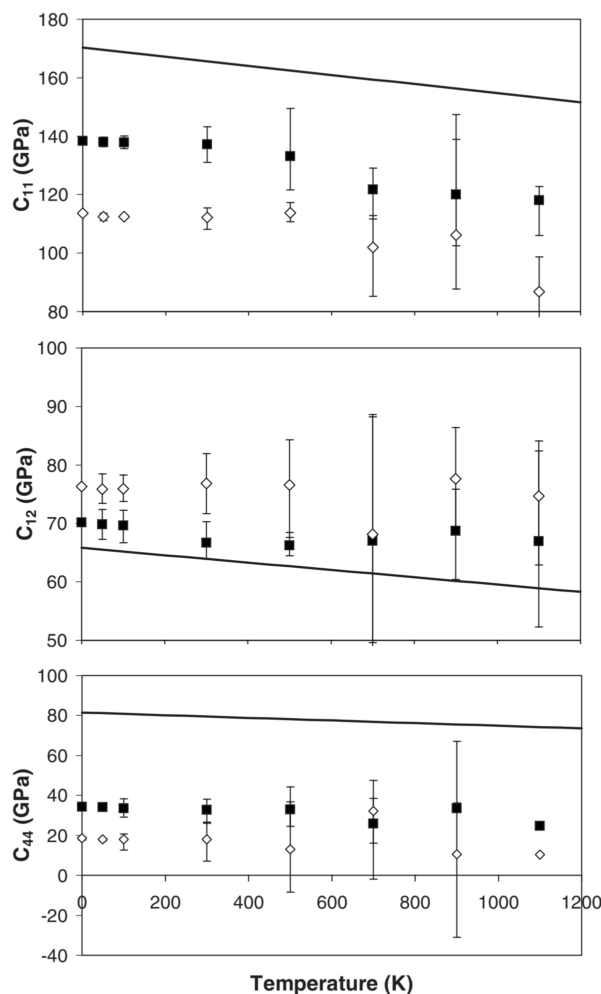


FIG. 13. Elastic constants calculated for 2B-Si (squares) and mXB (diamonds) for amorphous silicon. The error bars indicate high and low values. The solid line represents the experimental values for diamond-cubic silicon.[111]

at temperatures above 300 K. These values are much larger than the experimentally determined values or the values calculated with the 2B-Si potential.

The elastic constants of the amorphous silicon structures generated as described in Sec. III C (shown in Fig. 5) have been calculated as a function of temperature. The results are plotted in Fig. 13. Because mechanical property data for *a*-Si is somewhat limited, the experimental values for diamond-cubic silicon are given as a point of reference. It is expected that the elastic constants for diamond-cubic silicon and amorphous silicon should be similar in magnitude because both structures are largely tetrahedral. For the *a*-Si generated with the 2B-Si potential, both $C_{12}$ and $C_{44}$ are relatively independent of temperature while $C_{11}$ decreases slightly. The anisotropy factor calculated for the 2B-Si *a*-Si is relatively small, ranging between −0.001 and 0.07, and is independent of temperature suggesting that the amorphous structure is fairly isotropic.

## IV. SUMMARY

In this work, parameters for Si-Si interactions based on the second-generation REBO formalism (2B-Si) are presented. There are four reasons why we chose to develop a parameter set for Si-Si interactions within the second-generation REBO formalism rather than use one of the many existing Si empirical potentials. First, the REBO potential has been used extensively to model a wide range of processes. Parametrizations of many atom types exist. This work increases the number of atomic interactions that have been parametrized for this potential formalism. Second, the second-generation REBO does a reasonable job reproducing the zero-Kelvin elastic constants of diamond and graphite. This is a result of the way in which the angular function was fit. By using this same procedure, the elastic constants of diamond-cubic silicon were fit. Most empirical potentials for Si, with the exception of the EDIP, *T*3, and BOP, are unable to reproduce the zero-Kelvin elastic constants.[19,29] Third, the updated form of the angular part of the second-generation REBO for C-C interactions also produces the correct dependence of the elastic constants and bulk modulus of diamond with temperature[31] and improved the ability of the potential to reproduce the correct defect formation energies.[30] By extension, it seemed likely that the same would be true for a Si-Si parametrization within this formalism. Finally, because our ultimate goal is to model chemical reactions in C-, Si-, and H-containing systems, a bond-order potential that can model these atoms as well as combinations of these atoms is needed. Because C-C and C-H parameters have already been published, our parametrization of Si-Si interactions is another step toward having all the needed parameters to model C-, Si-, and H-containing systems within the second-generation formalism.

This new Si parametrization was used to calculate a wide range of values for crystalline silicon structures, amorphous silicon structures, and liquid silicon. Because we are ultimately interested in a potential that can model C, Si, and H, we have compared our new parametrization for Si with the mXB potential. Because the EDIP for Si is able to reproduce the zero-Kelvin elastic constants of diamond-cubic silicon, and because it produces a reasonable amorphous structure from the melt, we included the previously published values for the EDIP in this work for comparison. Available data for the recently published BOP for Si are also included for comparison because it predicts the correct Cauchy pressure for diamond-cubic silicon. These potentials are among the few that are able to model the elastic properties of diamond-cubic silicon correctly. Extensive comparisons of most other empirical silicon potentials have been published previously[15,29] and are, therefore, not included here.

The ability of the potential to model a realistic amorphous phase is important for the simulation of many C-, Si-, and H-containing systems, such as Si-doped diamondlike carbon. The 2B-Si is able to reproduce amorphous silicon properties which are in good agreement with experimentally determined properties and those from *ab initio* MD studies. The positions of the peaks in the pair-correlation function are in very good agreement with the experimentally determined values. The amorphous silicon produced from the melt is

dominated by tetrahedrally coordinated silicon as is the case in the samples produced with *ab initio* MD. In addition, a small number of $T3$ and $T5$ defects are found in the amorphous silicon. This also agrees with the findings of *ab initio* MD simulations and TB. The structures obtained with the 2B-Si are slightly better than those obtained using the mXB potential. For instance, the elastic constants for the amorphous structures are too low as was the case with the crystalline silicon structures. Moreover, no $T3$ defects were apparent in the structures obtained with mXB potential. The radial and bond-angle distributions obtained using the EDIP are in good agreement with experiment although no data on the elastic constants or defects were published. Lastly, data for the amorphous phase produced using the BOP are not available.

While the goals of this work, producing a Si-Si potential based on the second-generation REBO formalism that could model the elastic properties in crystalline and amorphous solids, were met, for completeness a wide variety of other materials properties were also calculated. For example, the cohesive energies, defect relaxation energies, lattice parameters, and bulk moduli for a wide range of crystalline Si structures, including structures that were not used in the fitting procedure, are also reproduced well by this new parametrization. With the exception of $C_{44}$, the zero-Kelvin elastic constants of diamond-cubic silicon are within 3% of the experimentally determined values. The 2B-Si potential does quite well reproducing energies of the ideal and relaxed (100) $(1\times1)$ and $(2\times1)$ surfaces. In addition, it is also able to reproduce the energies of the ideal and relaxed (111) $(1\times1)$ surfaces. However, it incorrectly predicts that adatom structures on the (111) surface are less stable than the ideal (111) surface. This problem is common among empirical potentials for silicon. In fact, only the $T2$ potential, examined by Balamane *et al.*,[29] and the mXB potential correctly predict that the adatom structures examined here are more stable than the ideal (111) $(1\times1)$ surface. Despite this, neither of those potentials correctly predicts the order of stability obtained with DFT.

Examination of structure of liquid silicon provides an interesting test of the transferability of the 2B-Si potential because it was not fit to any properties of the liquid (or the amorphous) phase. The 2B-Si potential is able to reproduce the experimentally determined pair-correlation function. In addition, the bimodal shape of the bond-angle distribution obtained in *ab initio* MD[80] simulations is also reproduced. However, in the distributions obtained with both the mXB and the 2B-Si, the most probable angle is shifted away from 90° closer to the tetrahedral angle. In addition, the melting point of the liquid is approximately two times larger than the melting point of silicon. The BOP reproduces the melting point of Si; however, data for the structure of the liquid phase were not reported.

Despite the various functional forms and fitting parameters for existing Si potentials, the discovery of one universal function form or parameter set that accurately describes all possible silicon structures and phases has remained elusive. Thus, a potential energy function should be chosen based on the processes one wishes to simulate. For example, there are potentials that are able to model the structure and energetics of silicon clusters or the properties of liquid silicon that are unable to simultaneously model bulk properties of crystalline and amorphous silicon. Some potential energy functions are able to reproduce the melting temperature of Si but do not predict the correct density of the liquid. The parametrization of the second-generation REBO for Si presented here is able to model a wide range of properties of both crystalline and amorphous Si. It is among two potentials that are able to reproduce a reasonable amorphous structure by melting Si. Like all empirical potentials published to date, it cannot reproduce all the properties for all phases of Si. Based on the analysis provided herein, this parametrization performed as well, or better, than previously published Si potentials in reproducing a wide range of properties in crystalline, amorphous, and liquid silicon. Current work is focused on the development of Si-C and Si-H parameters within this formalism. This will allow for reactive processes in a broad range of Si-, C-, and H-containing materials to be simulated.

## ACKNOWLEDGMENTS

J.D.S. and G.G. acknowledge support from AFOSR under Contracts No. F1ATA06306G001 and No. F1ATA053001G004 (Extreme Friction MURI), respectively. J.A.H. acknowledges support from the ONR and AFOSR under Contracts No. N0001406WR20205 and No. F1ATA06355G001, respectively. K. Van Workum, D. W. Brenner, S. B. Sinnott, and B. Ni are thanked for helpful discussions. We also thank M. Z. Bazant and J. Justo for providing EDIP data.

*To whom correspondence should be addressed, jah@usna.edu

[1] F. H. Stillinger and T. A. Weber, Phys. Rev. B **31**, 5262 (1985).
[2] J. Tersoff, Phys. Rev. Lett. **56**, 632 (1986).
[3] J. Tersoff, Phys. Rev. B **37**, 6991 (1988).
[4] J. Tersoff, Phys. Rev. B **38**, 9902 (1988).
[5] M. I. Baskes, Phys. Rev. Lett. **59**, 2666 (1987).
[6] M. I. Baskes, J. S. Nelson, and A. F. Wright, Phys. Rev. B **40**, 6085 (1989).
[7] B. C. Bolding and H. C. Anderson, Phys. Rev. B **41**, 10568 (1990).
[8] K. Beardmore and R. Smith, Philos. Mag. A **74**, 1439 (1996).
[9] R. Biswas and D. R. Hamann, Phys. Rev. B **36**, 6434 (1987).
[10] B. W. Dodson, Phys. Rev. B **35**, 2795 (1987).
[11] A. J. Dyson and P. V. Smith, Surf. Sci. **355**, 140 (1996).
[12] J. F. Justo, M. Z. Bazant, E. Kaxiras, V. V. Bulatov, and S. Yip, Phys. Rev. B **58**, 2539 (1988).
[13] C. Sbraccia, P. L. Silvestrelli, and F. Ancilotto, Surf. Sci. **516**, 147 (2002).
[14] B. A. Gillespie, X. W. Zhou, D. A. Murdick, H. N. G. Wadley, R. Drautz, and D. G. Pettifor, Phys. Rev. B **75**, 155207 (2007).
[15] S. J. Cook and P. Clancy, Phys. Rev. B **47**, 7686 (1993).
[16] J. Tersoff, Phys. Rev. B **39**, 5566 (1989).
[17] H. Balamane, T. Halicioglu, and W. A. Tiller, Phys. Rev. B **46**, 2250 (1992).

[18] N. A. Marks, Phys. Rev. B **63**, 035401 (2000).
[19] M. Z. Bazant, E. Kaxiras, and J. F. Justo, Phys. Rev. B **56**, 8542 (1997).
[20] D. G. Pettifor, Phys. Rev. Lett. **63**, 2480 (1989).
[21] D. G. Pettifor and I. I. Oleinik, Phys. Rev. Lett. **84**, 4124 (2000).
[22] D. G. Pettifor and I. I. Oleinik, Phys. Rev. B **59**, 8487 (1999).
[23] G. C. Abell, Phys. Rev. B **31**, 6184 (1985).
[24] D. W. Brenner, Phys. Rev. B **42**, 9458 (1990).
[25] D. W. Brenner, J. A. Harrison, C. T. White, and R. J. Colton, Thin Solid Films **206**, 220 (1991).
[26] M. V. Ramana Murty and H. A. Atwater, Phys. Rev. B **51**, 4889 (1995).
[27] D. Humbird and D. B. Graves, J. Chem. Phys. **120**, 2405 (2004).
[28] K. Albe, K. Nordlund, and R. S. Averback, Phys. Rev. B **65**, 195124 (2002).
[29] H. Balamane, T. Halicioglu, and W. A. Tiller, Phys. Rev. B **46**, 2250 (1992).
[30] D. W. Brenner, O. A. Shenderova, J. A. Harrison, S. J. Stuart, B. Ni, and S. B. Sinnott, J. Phys.: Condens. Matter **14**, 783 (2002).
[31] G. T. Gao, K. Van Workum, J. D. Schall, and J. A. Harrison, J. Phys.: Condens. Matter **18**, S1737 (2006).
[32] K. Van Workum, G. T. Gao, J. D. Schall, and J. A. Harrison, J. Chem. Phys. **125**, 144506 (2006).
[33] B. Ni, K. H. Lee, and S. B. Sinnott, J. Phys.: Condens. Matter **16**, 7261 (2004).
[34] S. P. Jordan and V. H. Crespi, Phys. Rev. Lett. **93**, 255504 (2004).
[35] P. Liu, Y. W. Zhang, and C. Lu, J. Appl. Phys. **98**, 113522 (2005).
[36] H. Ustunel, D. Roundy, and T. A. Arias, Nano Lett. **5**, 523 (2005).
[37] O. A. Shenderova and D. W. Brenner, Phys. Rev. B **60**, 7053 (1999).
[38] O. A. Shenderova and D. W. Brenner, Solid State Phenom. **87**, 205 (2002).
[39] O. A. Shenderova, D. W. Brenner, and L. H. Yang, Phys. Rev. B **60**, 7043 (1999).
[40] G. T. Gao, P. T. Mikulski, G. M. Chateauneuf, and J. A. Harrison, J. Phys. Chem. B **107**, 11082 (2003).
[41] G. T. Gao, P. T. Mikulski, and J. A. Harrison, J. Am. Chem. Soc. **124**, 7202 (2002).
[42] J. Samela, K. Nordlund, J. Keinonen, and V. N. Popok, Nucl. Instrum. Methods Phys. Res. B **255**, 253 (2007).
[43] P. A. Thompson and M. O. Robbins, Phys. Rev. A **41**, 6830 (1990).
[44] D. W. Brenner, Phys. Status Solidi B **217**, 23 (2000).
[45] D. W. Brenner, O. A. Shenderova, and D. A. Areshkin, in *Reviews in Computational Chemistry*, edited by K. B. Lipkowitz and D. B. Boyd (Wiley-VCH, New York, NY, 1998), Vol. 5, p. 207.
[46] M. W. Finnis and J. E. Sinclair, Philos. Mag. A **50**, 45 (1984).
[47] D. G. Pettifor and I. I. Oleinik, Phys. Rev. B **65**, 172103 (2002).
[48] MATHEMATICA, Version 5.2 (Wolfram Research, Inc., Champaign, IL, 2005).
[49] G. Katzer, M. C. Ernst, A. F. Sax, and J. Kalcher, J. Phys. Chem. A **101**, 3942 (1997).
[50] M. T. Yin and M. L. Cohen, Phys. Rev. Lett. **45**, 1004 (1980).
[51] M. T. Yin and M. L. Cohen, Phys. Rev. B **26**, 5668 (1982).
[52] M. T. Yin and M. L. Cohen, Phys. Rev. B **29**, 6996 (1984).
[53] N. Bernstein, M. J. Mehl, D. A. Papaconstatopoulos, N. I. Papanicolaou, M. Z. Bazant, and E. Kaxiras, Phys. Rev. B **62**, 4477 (2000).
[54] B. T. Colegrove and H. F. Schaefer III, J. Phys. Chem. **94**, 5593 (1990).
[55] G. Simmons and H. Wang, *Single Crystal Elastic Constants and Calculated Aggregate Properties: A Handbook* (MIT, Cambridge, MA, 1971).
[56] D. A. Murdick, X. W. Zhou, H. N. G. Wadley, D. Nguyen-Manh, R. Drautz, and D. G. Pettifor, Phys. Rev. B **73**, 045206 (2006).
[57] M. Born and K. Huang, *Dynamic Theory of Crystal Lattices* (Clarendon, Oxford, 1956).
[58] J. H. Wang, S. Yip, S. R. Phillpot, and D. Wolf, Phys. Rev. Lett. **71**, 4182 (1993).
[59] B. G. Pfrommer, M. Côté, S. G. Louie, and M. L. Cohen, Phys. Rev. B **56**, 6662 (1997).
[60] L. L. Boyer, E. Karxiras, J. L. Feldman, J. Q. Broughton, and M. J. Mehl, Phys. Rev. Lett. **67**, 715 (1991).
[61] O. H. Nielsen and R. M. Martin, Phys. Rev. B **32**, 3792 (1985).
[62] N. Bernstein and E. Kaxiras, Phys. Rev. B **56**, 10488 (1997).
[63] A. Fukumoto, Phys. Rev. B **42**, 7462 (1990).
[64] W. H. Press, S. A. Teukolsky, and W. T. Vetterling, *Numerical Recipies in FORTRAN* (Cambridge University Press, New York, NY, 1992).
[65] D. Haneman, Rep. Prog. Phys. **50**, 1045 (1987).
[66] R. J. Hamers, R. M. Tromp, and J. E. Demuth, Phys. Rev. B **34**, 5343 (1986).
[67] R. M. Tromp, R. J. Hamers, and J. E. Demuth, Phys. Rev. Lett. **55**, 1303 (1985).
[68] J. E. Northrup, Phys. Rev. Lett. **57**, 154 (1986).
[69] R. D. Meade and D. Vanderbilt, Phys. Rev. B **40**, 3905 (1989).
[70] S. D. Solares, S. Dasgupta, P. A. Schultz, Y. H. Kim, C. B. Musgrave, and W. A. Goddard, Langmuir **21**, 12404 (2005).
[71] M. Stutzmann and D. K. Biegelsen, Phys. Rev. Lett. **60**, 1682 (1988).
[72] K. E. Khor and S. Das Sarma, Phys. Rev. B **39**, 1188 (1989).
[73] J. E. Northrup and M. L. Cohen, Phys. Rev. B **29**, 1966 (1984).
[74] F. Wooten, K. Winer, and D. Weaire, Phys. Rev. Lett. **54**, 1392 (1985).
[75] N. Bernstein, J. L. Feldman, and M. Fornari, Phys. Rev. B **74**, 205202 (2006).
[76] D. A. Drabold, P. A. Fedders, O. F. Sankey, and J. D. Dow, Phys. Rev. B **42**, 5135 (1990).
[77] M. Fornari, M. Peressi, S. de Gironcoli, and A. Baldereschi, Europhys. Lett. **47**, 481 (1999).
[78] J. Fortner and J. S. Lannin, Phys. Rev. B **39**, 5527 (1989).
[79] S. T. Pantelides, Phys. Rev. Lett. **57**, 2979 (1986).
[80] I. Stich, R. Car, and M. Parrinello, Phys. Rev. B **44**, 11092 (1991).
[81] P. A. Fedders and A. E. Carlsson, Phys. Rev. Lett. **58**, 1156 (1987).
[82] J. C. Phillips, Phys. Rev. Lett. **58**, 2824 (1987).
[83] K. Laaziri, S. Kycia, S. Roorda, M. Chicoine, J. L. Robertson, J. Wang, and S. C. Moss, Phys. Rev. Lett. **82**, 3460 (1999).
[84] K. Laaziri, S. Kycia, S. Roorda, M. Chicoine, J. L. Robertson, J. Wang, and S. C. Moss, Phys. Rev. B **60**, 13520 (1999).
[85] J. S. Custer, M. O. Thompson, D. C. Jacobson, J. M. Poate, S. Roorda, W. C. Sinke, and F. Spaepen, Appl. Phys. Lett. **64**, 437 (1994).
[86] R. F. Wood, C. W. White, and R. T. Young, in *Semiconductors and Semimetals* (Academic, New York, 1984), Vol. 23.
[87] G. DeSandre, L. Colombo, and C. Bottani, Phys. Rev. B **54**, 11857 (1996).
[88] Y. Bar-Yam and J. D. Joannopoulos, Phys. Rev. Lett. **56**, 2203

(1986).
[89] M. Ishimaru, K. Yoshida, T. Kumamoto, and T. Motooka, Phys. Rev. B **54**, 4638 (1996).
[90] A. D. Mistriotis, N. Flytzanis, and S. C. Farantos, Phys. Rev. B **39**, 1212 (1989).
[91] S. Ansell, S. Krishnan, J. J. Felten, and D. L. Price, J. Phys.: Condens. Matter **10**, L73 (1998).
[92] M. Sprik, R. W. Impey, and M. L. Klein, Phys. Rev. B **29**, 4368 (1984).
[93] J. R. Ray, Comput. Phys. Rep. **8**, 109 (1988).
[94] J. R. Ray, M. C. Moody, and A. Rahman, Phys. Rev. B **32**, 733 (1985).
[95] M. S. Daw and M. I. Baskes, Phys. Rev. B **29**, 6443 (1984).
[96] J. R. Ray and A. Rahman, J. Chem. Phys. **82**, 4243 (1985).
[97] K. Van Workum and J. J. de Pablo, Nano Lett. **3**, 1405 (2003).
[98] K. Van Workum and J. J. de Pablo, Phys. Rev. E **67**, 011505 (2003).
[99] K. Van Workum and J. J. de Pablo, Phys. Rev. E **67**, 031601 (2003).
[100] C. Kittel, *Introduction to Solid State Physics* (John Wiley & Sons, Inc., New York, 1971).
[101] P. J. Fay and J. R. Ray, Phys. Rev. A **46**, 4645 (1992).
[102] A. A. Gusev, M. M. Zehnder, and U. W. Suter, Phys. Rev. B **54**, 1 (1996).
[103] H. Goldstein, *Classical Mechanics*, 2nd ed. (Addison-Wesley, Reading, MA, 1980).
[104] W. Smith, CCP5 Quarterly **10**, 37 (1983).
[105] M. Parrinello and A. Rahman, Phys. Rev. Lett. **45**, 1196 (1980).
[106] S. Nosé and M. L. Klein, Mol. Phys. **50**, 1055 (1983).
[107] C. W. Gear, *Numerical Initial Value Problems in Ordinary Differential Equations* (Prentice-Hall, Englewood Cliffs, CA, 1971).
[108] S. Nosé, Mol. Phys. **52**, 255 (1983).
[109] *Properties of Crystalline Silicon*, edited by R. Hull (Institution of Electrical Engineers, London, 1999).
[110] B. Yates, *Thermal Expansion* (Plenum, New York, 1972).
[111] *Group III Condensed Matter* (Springer, Landolt-Börnstein, Group III Condensed Matter, 41/A1A (Springer, Berlin (2001).